Mid-crustal strain localisation triggered by localised fluid influx and activation of dissolution-precipitation creep

Authors: Manon Carpenter (eemrca@leeds.ac.uk), Sandra Piazolo, Tim Craig and Tim Wright All authors are affiliated with the University of Leeds.

This paper is a non-peer reviewed preprint submitted to EarthArXiv.
It has been submitted to the Journal of Structural Geology and is in review.

Mid-crustal strain localisation triggered by localised fluid influx and activation of dissolution-precipitation creep

Manon Carpenter[a,1], Sandra Piazolo[a], Tim Craig[a], Tim Wright[a]

[a] *University of Leeds, Woodhouse, Leeds, LS2 9JT, UK*

Abstract

To understand how the mid-crust deforms is vital in understanding the spatial and temporal distribution of strain localisation, with implications for upper-crust deformation including seismic hazard. Here, we conduct fieldwork and microstructural and chemical analyses on the amphibolite-facies, 100-m-wide Upper Badcall shear zone in northwest Scotland, which deforms initially anhydrous quartzofeldspathic gneiss and a mafic dyke. We show that with increasing strain, m-scale strain distribution and mineral chemistry become increasingly homogeneous, while hydrous phases and syn-deformational quartz veins become more abundant. With increasing strain there is an overall increase in grain size, grain boundary alignment and shape preferred orientation in amphibole, plagioclase and quartz. Only amphibole and large grained quartz exhibit crystallographic preferred orientation in strained areas. Subtle microstructures that may be overlooked elsewhere, particularly in felsic gneiss, indicate dominant activity of dissolution-precipitation creep and equivalent rheological weakening in both mafic and felsic rocks. We interpret that brittle fractures in anhydrous crust allow localised fluid-infiltration, which triggers retrogressive metamorphic reactions and introduces sufficient

grain boundary fluid for deformation to favour dissolution-precipitation creep over dislocation creep. Our study suggests that deformation by dissolution-precipitation creep may be more dominant in mid- to lower-crustal localised zones of deformation than previously thought.
Keywords: Strain localisation, Dissolution-precipitation creep, Mid-crust rheology, Fluid-rock interaction

1. Introduction

The majority of displacement accumulated in the mid- to lower-continental crust is accommodated in shear zones, the ductile counterparts of brittle faults in crustal-scale structures, where strain is higher than in the surrounding wall rock (Sorensen, 1983; Henstock et al., 1997; Yamasaki et al., 2014; Clerc et al., 2015; Fagereng et al., 2024). Knowing the mechanisms associated with strain localisation is a vital step towards understanding how and where significant crustal deformation and hazards such as earthquakes occur. To localise strain in discrete zones requires a localised weakening mechanism. Such a weakening process is likely to be the result of a dynamic combination of factors depending on the geological setting, involving an interplay between ductile and brittle deformation (e.g., Rutter and Brodie, 1985; Bürgmann and Dresen, 2008; Brander et al., 2012; Corvò et al., 2021).

We know the rheology of deforming mid- to lower-continental crust is predominantly viscous, based on observations of exhumed mm to km scale shear zones (Ramsay and Graham, 1970; Carreras and Casas, 1987; Carreras, 2001; Svahnberg and Piazolo, 2010; Gerbi et al., 2016) and geophysical observations (Kaufmann and Amelung, 2000; Kenner and Segall, 2003; Bürgmann and Dresen, 2008; Weiss et al., 2019). Experiments have long been used to determine the governing flow laws that can describe the viscous deformation observed in these regions (e.g., Rybacki and Dresen, 2000; Hirth and Kohlstedf, 2003). However, two overarching questions remain, namely (1) what controls why strain localises in discrete zones and (2) which deformation mechanisms are dominant in these zones. Only if we know the dominant deformation mechanisms active in these localised, discrete zones, is it possible to predict and/or reconstruct the form of the appropriate flow law by which the rocks deform (e.g. linear-viscous versus power-law). With appropriate flow laws we can build geophysical models that enable us to interpret geodetic data, in which observations of active fault zones are short-term snapshots of time-varying deformation (e.g., Hussain et al., 2018; Takeuchi and Fialko, 2012; Yamasaki et al., 2014).

Previous studies have put forward a number of candidate models to explain how strain localises in shear zones (for review see Fossen and Cavalcante, 2017, and references therein). For example, deformation dominated by dislocation creep follows a power-law flow law which enables strain localisation (cf. Equation 1, stress exponent $n \geq 3$). In addition, localised weakening may occur if associated dynamic recrystallisation weakens rock through grain size reduction, which subsequently drives a switch to grain-size-sensitive deformation mechanisms where grain size is small (e.g., Kirby, 1985; Drury, 2005; Warren and Hirth, 2006; Svahnberg and Piazolo, 2010). Shear zones may also initiate due to rock heterogeneity at macro or micro scale (Handy, 1994; Dell'Angelo and Tullis, 1996; Ingles et al., 1999; Mandal et al., 2004), including fractures or joints and dykes (Segall and Simpson, 1986; Pennacchioni and Mancktelow, 2007; Smith et al., 2015), or rheological contrasts between different lithologies (e.g., Corvò et al., 2022). Extrinsic factors may also play a role, for example, if fluid introduction weakens rock through hydrous metamorphic reactions that lead to softening through mineral assemblage change (Teall, 1885; Ramsay and Graham, 1970; Beach, 1980; Rutter and Brodie, 1985; Moore et al., 2020; Bras et al., 2021) and/or reaction-driven grain size reduction (Kirby, 1985; Stünitz and Tullis, 2001;

Smith et al., 2015; Soret et al., 2019; Stenvall et al., 2019; Mansard et al., 2020). The dominance of different weakening and hardening mechanisms may continuously change as the deformation history develops, and therefore specific rheological behaviour may be transient (Rutter et al., 2001; Steffen et al., 2001; Gardner et al., 2017a; Bras et al., 2021, and references therein). Switches in the dominant mechanism can occur by changes in the extrinsic and intrinsic parameters such as temperature, fluid availability, stress, and grain size (e.g., Kirby, 1985; Rutter and Brodie, 1988; Viegas et al., 2016). Such transient rheological behaviour of the crust may be reflected in geophysical observations of active faults, with increasingly long observation periods now showing a range of transient processes in the mid- to lower-crust following larger earthquakes (e.g. Weiss et al., 2019; Tian et al., 2020).

An experimentally-derived flow law that describes the relationship between strain rate and stress can be written in the general form

$$\dot{\varepsilon} = A d^{-m} \sigma^{n} \exp\left(-\frac{Q}{RT}\right) \tag{1}$$

Where $\dot{\varepsilon}$ is strain rate, A is a material constant, d is the average grain size and m is the grain size exponent, σ the stress difference (in a triaxial setup) and n is the stress exponent, Q is activation energy, R is gas constant and T is absolute temperature (Ranalli, 1997). A and Q are material constants which vary depending on rock type and water content. Exponents m and n depend on the specific mechanism by which the material is deforming. The dominant deformation mechanism active in the mid-crust is commonly thought to be dislocation creep (Bürgmann and Dresen, 2008, and references therein). This is based on observations of quartz- and feldspar-rich natural shear zones (e.g., Kruse and Stünitz, 1999; Stipp et al., 2002; Piazolo and Passchier, 2002; Czaplińska et al., 2015; Lusk and Platt, 2020; Orlandini and Mahan, 2020) and experiments (e.g., Hirth and Tullis, 1994). Dislocation creep shows no grain size dependence ($m = 1$); it is grain size insensitive. The stress exponent n is generally between 3-5 (Schmid et al., 1980; Boland and Tullis, 1986; Carter et al., 1993; Karato and Wu, 1993) resulting in a power-law rheology (aka power-law creep). Inherent to a non-Newtonian power-law rheology is the localisation of strain (e.g., Carreras et al., 1977; Ranalli, 1995; Moore and Parsons, 2015). This mechanism is dominant at medium to high stresses and medium to high temperatures, hence is often associated with mid-crustal deformation (see review by Gomez-Rivas et al. 2020 and references therein).

The microstructural signatures of dislocation creep include bent crystal lattices within individual grains, seen optically as undulous extinction, the formation of subgrains, grain size reduction by subgrain rotation (dynamic recrystallisation), crystallographic preferred orientation (CPO), heterogeneous nucleation and core mantle structures (Trimby et al., 1998; Prior et al., 2002; Piazolo et al., 2002; Passchier C and Trouw R, 2005; Halfpenny et al., 2006). Because dislocation creep can be active at medium to high stresses and temperatures, without the need for fluids, it has historically been considered the dominant deformation mechanism in the mid- to lower-crust where fluids are thought to be scarce (Rutter, 1976; Gratier et al., 2013). Estimates of the strength of Earth's crust are generally based on dislocation creep-deformed grain size pietzometry (Twiss, 1977; Cross and Skemer, 2019; Goddard et al., 2020; Tokle and Hirth, 2021; Platt et al., 2015).

At small enough grain sizes, the dominant deformation mechanism may switch to one that is grain size sensitive. The nature of the grain-size-sensitive deformation mechanisms has been the subject of a large number of studies over the last 20 years. Commonly, grain boundary sliding is thought to be associated with these processes. The flow law for grain boundary sliding accommodated by grain-size-sensitive diffusion creep exhibits a stress exponent $n = 1$, or, if accommodated by dislocation glide, then $n = 2$ (Nieh and Wadsworth, 1997; Dimanov et al., 2007). As such, the deforming material behaves in a Newtonian viscous manner and, in the absence of additional factors, is inherently unable to localise strain due to the linear relationship between stress and strain rate. Based on observations of high strain quartz-, feldspar- or calcite-dominated rocks, signatures for grain-size-sensitive flow attributed to grain boundary sliding accommodated by dislocation glide or diffusion creep (DisGBS) include: random misorientation axes and weakening of any existing CPO (Jiang et al., 2000; Bestmann and Prior, 2003), low internal grain deformation and equant grains (Passchier C and Trouw R, 2005; Wightman et al., 2006), and phase mixing (e.g., Kruse and Stünitz, 1999; Warren and Hirth, 2006; Dimanov et al., 2007). Because DisGBS is grain-size-sensitive, where a contrast in grain size exists, strain partitioning can preserve large grains (e.g. porphyroclasts) where smaller grains preferentially accommodate strain (Warren and Hirth, 2006). Fusseis et al. (2009) suggest that in a polymineralic rock, grain boundary sliding accommodated by diffusion may result in fluid influx and migration based on their model of a fluid pump evoking localised and dynamic porosity generation.

An alternative deformation mechanism in the crust, which requires the presence of fluids, is dissolution-precipitation creep (aka pressure solution), which is a major mechanism of ductile deformation in the upper crust and is accepted to be an important process in the formation of cleavage (Gratier, 1987; Wheeler, 1992; Gratier et al., 2013; Putnis, 2021). The rheological flow law for dissolution-precipitation creep is generally accepted to be Newtonian, with a stress exponent n close to 1, and grain size sensitive (m = 3, Rutter, 1976; Gratier et al., 2023).

Reported signatures of dissolution-precipitation creep include truncation of grains and zoning, embayed/indented grain boundaries and preferential overgrowths, tails, or beards in the pressure shadows of large grains, which may be chemically distinct (Knipe, 1989; Wintsch and Yi, 2002; Stokes et al., 2012; Gratier et al., 2013; Wassmann and Stöckhert, 2013). In addition, coeval metamorphic reactions may occur which lead to phase changes during deformation (Stünitz et al., 2020; Malvoisin and Baumgartner, 2021; Lee et al., 2022). Shape preferred orientation (SPO) may develop in a differential stress field where the transportation rate of material is faster than precipitation (Malvoisin and Baumgartner, 2021). While Knipe (1989) suggested there will be a lack of CPO for minerals such as quartz, it has been shown that in fact elastically highly anisotropic minerals are predicted to dissolve preferentially in the elastically strong direction and grow preferentially in the weaker elastic direction. In this case, during pressure solution a SPO and CPO will develop (Kamb, 1959). This effect has been documented in nature by Wenk et al. (2020) in the highly elastically anisotropic mineral muscovite. Where dissolution-precipitation creep with anisotropic growth is modelled numerically, both a CPO and SPO is produced (Bons and Den Brok, 2000). Less elastically anisotropic minerals (i.e quartz) produce random CPO in similar studies (Wenk et al., 2020). In contrast to common reports of dissolution-precipitation creep at upper crustal levels, studies interpreting deformation in the mid- to lower-crust dominated by this mechanism remain relatively scarce. However, in recent years an increasing number of studies have identified the role of dissolution-precipitation creep in the mid- to lower-crust. These include cm- to m-scale shear zones (Díaz Aspiroz et al., 2007; Menegon et al., 2008; Giuntoli et al., 2018; Lee et al., 2022; Moore et al., 2020, 2024) and uniformly deformed km-scale units (amphibolite, Stokes et al. 2012; gneiss, Wintsch and Yi 2002). Yet to be widely documented is the role of dissolution-precipitation creep in shear zones larger than m-scale in the mid- to lower-crust. Whether this scarcity is a true reflection of the scarcity of this process in mid-crustal strain localisation, or rather a lack of widespread recognition of this process, remains unclear.

To address this gap in our knowledge, and assess by what process dissolution-precipitation creep may be a viable mechanism for strain localisation in the mid-crust, we investigate in detail the 100-m-wide, amphibolite-facies Upper Badcall shear zone in NW Scotland which deforms originally dry, lower-crustal, Archean granulite-facies rocks cross-cut by a mafic dyke (Beach et al. 1974; Coward and Potts 1983 and references therein; Tatham and Casey 2007; Fig 1). This shear zone is ideally suited for our study as it is well constrained in terms of accumulated strain, and its exceptional exposure allows for detailed strain mapping and sampling. Our field, microstructural and geochemical study shows that this shear zone deformed predominantly by dissolution-precipitation creep. We interpret that the necessary availability of grain boundary fluid was enabled by fluid infiltration through localised brittle fractures into previously dry, dislocation creep-deformed rock. Hydration does not only trigger retrogressive metamorphic reactions, but allows deformation to favour dissolution-precipitation creep over dislocation creep where enough fluid is present.

2. Geological setting and sample locations: Upper Badcall shear zone in the Lewisian Gneiss Complex

The Upper Badcall shear zone is situated within the Archean Assynt terrane, which comprises part of the Central Region of the Lewisian Gneiss Complex (LGC), northwest Scotland (Fig 1, Peach 1907; Sutton and Watson 1950; Friend and Kinny 2001; Kinny et al. 2005). Granulite-facies, pyroxene bearing gneisses formed during an early, 'Badcallian' event (previously known as 'Scourian' granulites, Sutton and Watson 1950; Park 1970; c. 2800 Ma Chapman and Moorbath 1977; Hamilton et al. 1979). This gneiss was deformed and retrogressed to hornblende- and biotite gneisses at amphibolite-facies conditions during either, or both, the 'Inverian' amphibolite-facies event (Evans 1965, c. 2490-2480 Ma, Friend and Kinny 1995), or the 'Laxfordian' amphibolite-facies event (c. 1750 Ma, Moorbath et al. 1969; Kinny and Friend 1997). The latter 'Laxfordian' event is identified where deformation truncates the mafic, predominantly dolerite, Scourie dyke swarm which intruded under conditions of 450–500°C and 500–700 MPa, at 2400-1900 Ma (Tarney, 1963) between the Inverian and Laxfordian events (Sutton and Watson, 1950; Park and Tarney, 1987).

The shear zone at Upper Badcall is part of a population of 'Laxfordian',

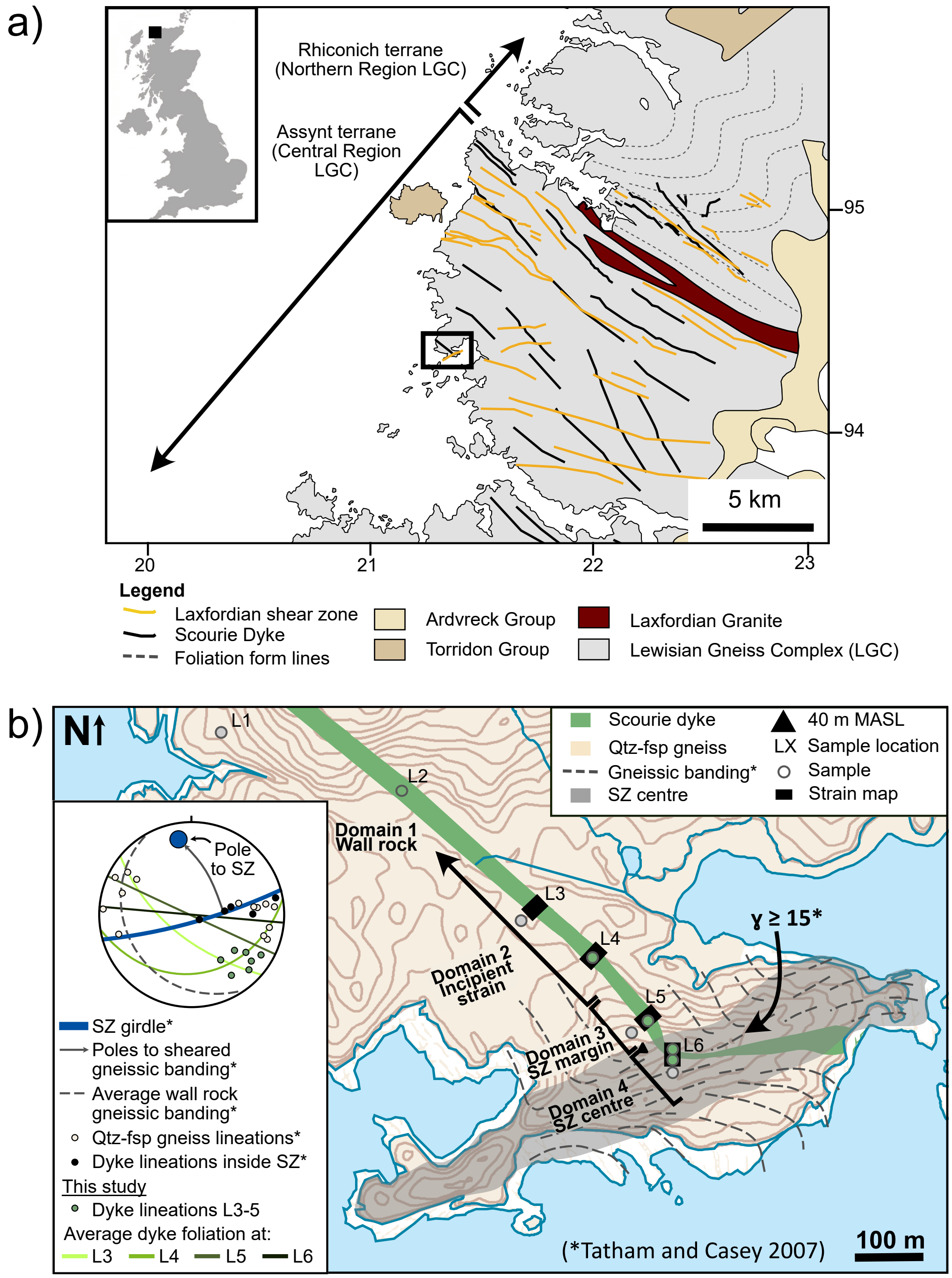

Figure 1: The geological setting of the field area in NW Scotland, UK; (a) Overview geological map of the Central Region of the Lewisian Gneiss Complex (LGC), modified after Beach (1974b), Beach et al. (1974) and Goodenough et al. (2010). Black box shows the location of the field area, and the co-ordinate system is British National Grid. Inset: Overview map of the UK. (b) Field area in Upper Badcall, showing the mafic Scourie dyke and surrounding quartzofeldspathic gneiss deformed into the shear zone, after Tatham and Casey (2007). MASL: Meters Above Sea Level.

amphibolite-facies shear zones seen across the Assynt terrane which deform both the gneisses and Scourie dykes (Fig 1a). These include 1-100 m discrete, steeply dipping shear zones (Beach et al., 1974; Goodenough et al., 2010) and km-wide structures (Laxford, aka Tarbet, Shear Zone, Beach et al. 1974; Goodenough et al. 2010; and Canisp, aka Stoer, Shear Zone, Attfield 1987). Beach (1974b) estimates a total of 22.5 km of horizontal displacement across these shear zones. This Laxfordian tectonometamorphism occurred at mid-crustal amphibolite-facies conditions estimated at 510–660°C and 5–8 kbar in the Assynt terrane (Beach, 1973; Cartwright, 1990; Pearce and Wheeler, 2014).

The Upper Badcall shear zone is approximately 100 m wide, trending ENE-WSW with subvertical foliation formed at angle to the gneissic foliation in the wall rock (Fig 1b). The shear zone deforms both the gneiss wall rock and a $\sim$ 10 m wide, near vertical Scourie dyke, in a ductile zone of oblique left-lateral strike slip which offsets the dyke by c. 190 m (Tatham and Casey, 2007). In the same study the authors calculate a shear strain by simple shear of at least 15 at the shear zone centre, based on the deflection of fabric in the surrounding gneisses. We present results from both gneiss and dyke which we sampled at varying distances along a general transect from 500 m from the shear zone centre, where amphibolite-facies deformation and recrystallisation is minimal, to the shear zone centre itself. Our samples represent the variation in strain along this transect (Fig 1; Table S1 in Supplementary data).

3. Methods

3.1. Thin section preparation and optical analysis

Samples are cut perpendicular to foliation (XY) and parallel to the lineation (X) where present, and polished down to $\sim 30\ \mu m$ thickness. Thin sections were first evaluated using a petrographic optical microscope. We obtained overview thin section scans using plustek OpticFilm 8100 scanner at 7200 resolution and photomicrographs using GXCAM HiChrome-HR4 camera and GX Capture imaging software. For quantitative orientation analyses using electron backscatter diffraction analysis (EBSD), samples were polished for a further 9 minutes using a colloidal silica-water solution. Samples were coated with a 5 nm and 10 nm thick carbon coat for EBSD analysis, and backscattered electron (BSE), cathodoluminesence (CL) imaging, and electron microprobe analysis (EMPA), respectively.

3.2. Electron microscope based techniques

3.2.1. Cathodoluminescence imaging

CL imaging of quartz microstructures was carried out using a Tescan VEGA3 XM at Leeds Electron Microscopy and Spectroscopy centre (LEMAS, University of Leeds, UK). The imaging was performed at high-vacuum conditions with an accelerating voltage of 20 kV and a working distance of 15 mm.

3.2.2. Quantitative crystallographic orientation analysis (EBSD) with qualitative mineral chemistry (EDX)

Simultaneous crystallographic orientation (EBSD) and qualitative mineral chemistry (EDX) data was collected using a FEI Quanta 650 SEM at

LEMAS equipped with the CMOS Symmetry EBSD detector, and X-Max 80 mm^2 EDX detector using AZtec software, all from Oxford Instruments. Analyses were performed at high-vacuum conditions with an accelerating voltage of 30 kV, a working distance of around 25 mm on a specimen tilted by 70°. Data was acquired on a regular grid. Large area maps (3 μm step size) were obtained for each sample, and small area, higher spatial resolution maps (1.5 μm step size) were obtained to observe finer features. The orientation data were then processed using AZtecCrystal software (Oxford Instruments).

The obtained EBSD maps contained 10-20 % non-indexed pixels (zero solutions), mostly resulting from the difficulty to index phyllosilicates, sericite-altered plagioclase and grain boundaries. We 'cleaned' data in AZtecCrystal to remove wild spikes (single pixels with incorrect phase ID), iteratively re-allocate zero solution pixels from neighbour orientations, and to rotate pixel data which shows pseudo-symmetry. Grains are defined by a minimum grain boundary angle of 10° and subgrains are defined by a boundary angle of 2–10° in intra-grain regions. After the processing procedure indexing exceeds 90 % in all maps except for AS2151 where 83 % pixels are indexed. Unless stated otherwise, pole figures are plotted with one pixel per grain as an equal area, upper hemisphere projection stereonet. To determine the shape orientation of grains we plot the fitted ellipse angle for the three main phases in both the dyke and gneiss (plagioclase, amphibole and quartz), with the X-axis in maps oriented 90-270°, and Z-axis oriented 0-180°, normal to foliation. To assess the internal deformation of grains we use cumulative disorientation profiles across individual grains, including subgrains where relevant, and grain relative orientation deviation (GROD) maps where for each grain the mean orientation is calculated and a colour scheme is used to show the deviation of each analysis points' crystallographic orientation relative to the mean crystallographic orientation.

For grain size (equivalent circle diameter) calculations, we disregarded twins both in quartz and plagioclase. We present grain size as both standard and area-weighted fraction. In both the gneiss and dyke wall rock, the large grains are so few by number that they do not alter the standard grain size results significantly; however, area-weighted fraction grain size histogram shows 2 distinct populations present in at least the wall rocks. To highlight these populations, we separate the main phase grain populations into small and large grain subsets, determined using area-weighted fraction grain size graphs. In the dyke small grains for each phase are: amphibole $> 200\ \mu m$, plagioclase $> 300\ \mu m$ and quartz $> 100\ \mu m$ equivalent circle diameter (plus all clinopyroxene which are max $90\ \mu m$). In the gneiss small grains for each phase are plagioclase $< 200\ \mu m$, quartz $< 100\ \mu m$ and amphibole $< 120\ \mu m$ equivalent circle diameter). So-called large grains are those above these values.

3.2.3. Mineral abundance estimates

We estimate mineral abundance using AZtecCrystal large area phase maps, plus AZtecCrystal EDX maps to estimate minerals that did not index well or at all (e.g. chlorite, biotite and muscovite). Estimates from phase maps and EDX have been cross-checked with overall mineral proportions present in thin section scale. Abbreviated mineral names follow the database from Whitney and Evans (2010), unless stated otherwise.

3.2.4. EDX data processing: Relative chemistry difference in plagioclase

To obtain relative and spatial chemistry difference between plagioclase compositions present in the gneiss and dyke we reconstructed EDX spectra for 1-3 mm^2 areas using TrueMap in AZtec, and obtained element abundance by stoichiometry combined with oxygen, normalised and reported as oxide%. Analysis data is available in Supplementary data Table S2. We report plagioclase compositions as relative weight fractions:

$$\#\text{Ab or } \#\text{An} = \frac{X\text{Ab or An}}{X\text{Ab} + X\text{An}} \tag{2}$$

Where

$$X\text{Ab} = \frac{\text{Na}_2\text{O wt\%}}{\text{MW of Na}_2\text{O}} \times \frac{\text{Molar proportion of Na}_2\text{O in albite}}{100} \tag{3}$$

And

$$X\text{An} = \frac{\text{CaO wt\%}}{\text{MW of CaO}} \times \frac{\text{Molar proportion of CaO in anorthite}}{100} \tag{4}$$

Relative difference EDX maps are produced in AZtecCrystal using Windows Integral data type, which is processed using a smoothing level of 2pix, auto stretch 20 % and smoothing method median filter.

3.2.5. Electron Microprobe Analysis (EMPA)

Quantitative chemical point analyses were obtained using a Jeol 8230 microprobe at LEMAS, with a 15-20 kV accelerating voltage, 10 nA beam current and a 1-5 μm spot size. The instrument was calibrated using standards WRS1485 amphibole and Kakanuii Hornblende for amphibole, and

SPH1, SKL1 and SKBy1 for plagioclase analysis. Analysis data is available in Supplementary data Tables S3 and S4. Areas of large amphibole grains containing ilmenite inclusions, and areas of plagioclase grains which are pock-marked sericite, were avoided. Where clear surfaces survived in the clay-altered plagioclase, intergrowth light and dark inclusions on 1-5 μm scale exist. These could not be avoided and resulted in a mixed signal and scattered data points. These points we disregarded in our analyses.

4. Results

4.1. General field relationships and outcrop characteristics

The mafic, now metamorphosed, dyke forms a low ridge that strikes NW/SE to the NW of the shear zone, and the quartzofeldspathic gneiss outcrops as patches amongst low vegetation (Fig 2a i). The shear zone coincides with a topographic high that reaches 40 m elevation above the surrounding coastline (Fig 1b; Fig 2a ii). Lineations within the dyke are object lineations (Piazolo and Passchier, 2002), including both amphibole grain and plagioclase aggregate lineations. Lineations rotate from plunging $\sim$ 20-40° SE outside the shear zone to plunging $\sim$ 20-40° E in the shear zone centre (Fig 1b). In general there is an increase in the number of small and discontinuous (0.5-20 mm wide, up to 60 cm long) quartz veins in the dyke with increasing proximity to the shear zone centre. The veins are parallel to subparallel to the fabric and exhibit a range of geometries from planar to isoclinally folded (axial plane parallel to deformation fabric).

Over 500 m NW from the shear zone centre the dyke is undeformed with an isotropic fabric defined by $\sim$ 60 % black amphibole and $\sim$ 40 % white pla-

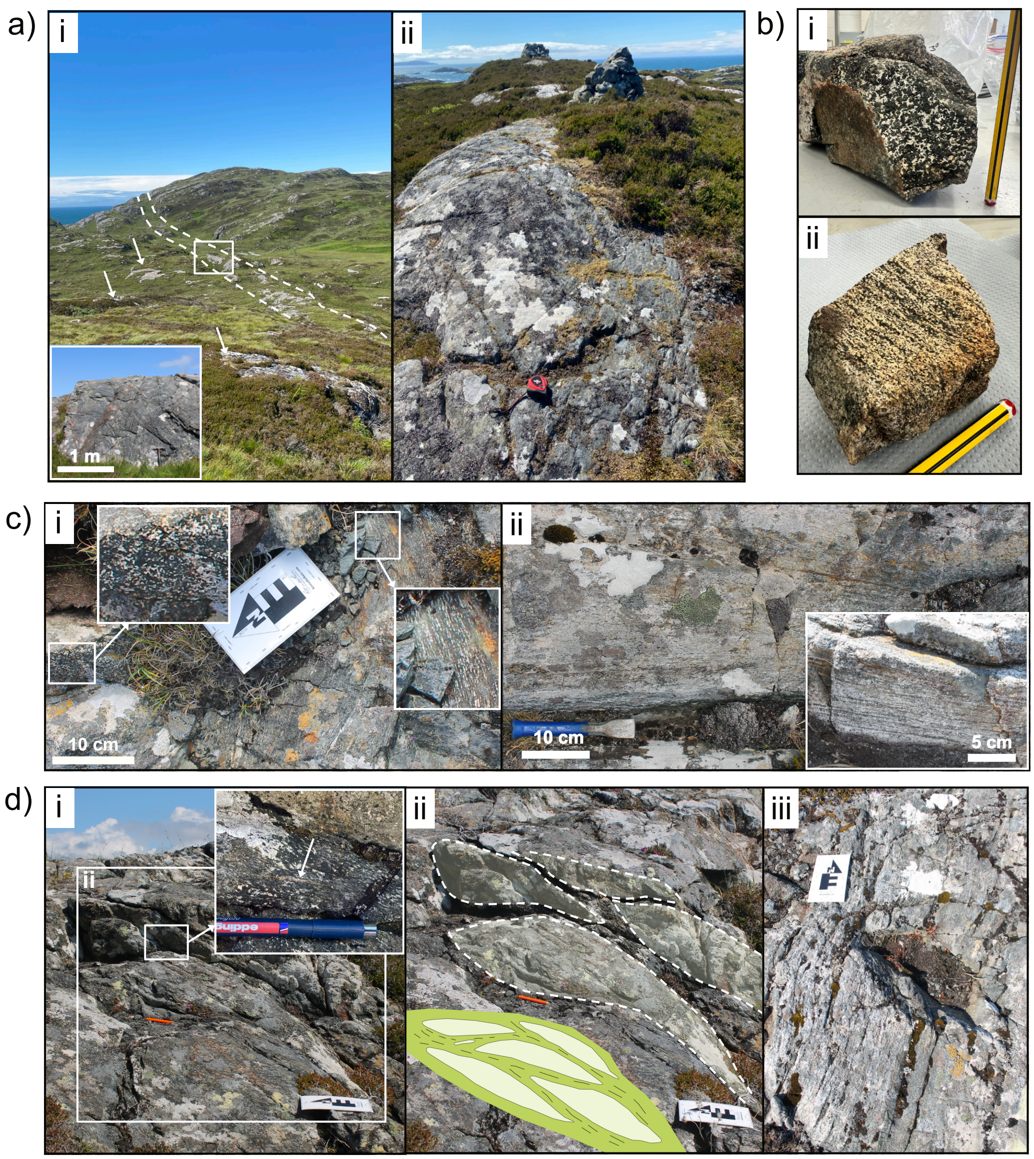

Figure 2: Photos showing an overview of the field area and outcrop or hand samples from > 200m from shear zone centre. (a) i) Looking NW over field area from shear zone centre, dashed lines trace dyke outcrop and white arrows indicate gneiss outcrop. Inset: dyke outcrop 350 m NW of shear zone (L3). ii) Looking W from shear zone centre. (b) Samples collected over 500 m from shear zone centre of i) dyke (L2) and ii) gneiss (L1), note cm-wide light and dark bands. (c) 350 m NW of shear zone centre (L3) showing i) dyke shape fabric variation and ii) gneiss. (d) 250 m NW of shear zone centre (L4) i) lenses of relatively undeformed dyke enveloped by anastomosing deformed dyke. Inset: singular quartz vein in band of low strain fabric. ii) annotated version and schematic illustration of (d) i), and iii) gneiss.

gioclase in 1-10 mm clusters (L2, Fig 1b; Fig 2b i). The quartzofeldspathic gneiss (L1) exhibits equant 1-3 mm grains and a weakly banded fabric (Fig 2b ii). Between 350 m (L3) and 250 m (L4) NW of the shear zone centre, elongate lenses of undeformed dyke are enveloped by anastomosing bands of deformed dyke which exhibits a shape fabric, defined by aligned, elongate plagioclase clusters, that varies in strength over a cm- to m-scale, perpendicular to fabric strike (Fig 1b; Fig 2c i & d i-ii). Rarely, singular, mm wide quartz veins are present, subparallel to the deformation fabric (Fig 2d i inset). The gneiss has a stronger fabric, defined by a few mm-cm wide alternating bands of plagioclase and amphibole, and contains discontinuous bands of quartz a few cm long (Fig 2c ii & d iii).

Approximately 100 m NW from the shear zone centre (L5) more than 50 % of the dyke is deformed and the shape fabric is dominantly planar, steeply dipping (290/80° NE) and continuous on a m-scale perpendicular to strike, rather than anastomosing around undeformed lenses (Fig 3a i). Within the deformed areas of the dyke multiple subparallel quartz veins are observed, $\sim$ 1-2 mm wide and up to 60 cm long (Fig 3a ii). The gneiss has a strong planar fabric defined by mm-cm wide light quartz and plagioclase, and less frequent dark mm-wide amphibole bands (Fig 3a iii).

In the shear zone centre the dyke is entirely deformed and both the dyke and gneiss have a pervasive, planar, steeply dipping (80-90°) fabric which strikes E/W and a lineation that plunges 20-40° E. The dyke-gneiss contact is also planar, concordant with the gneiss and dyke fabric, and shows no rheological contrast features such as boudinage or pinch and swell structures (Fig 3b i). The gneiss is weathered grey, similar to outside the shear zone,

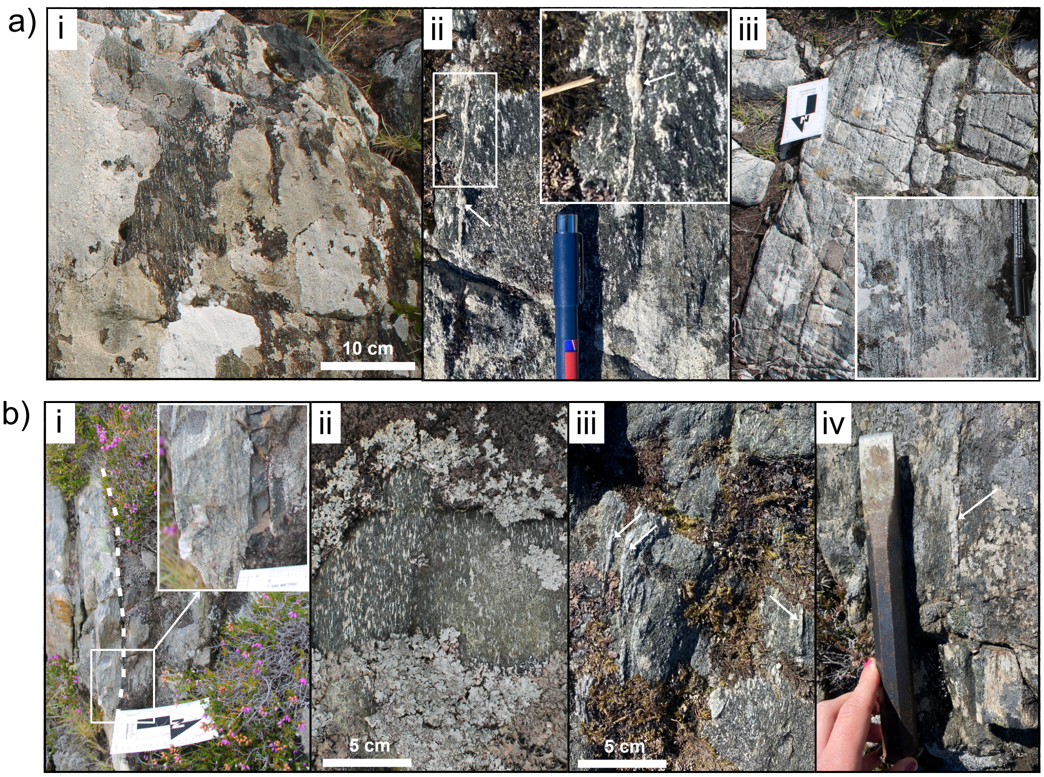

Figure 3: Photos of outcrops within 100 m of shear zone centre. (a) 100 m NW of shear zone centre; i) dyke looking SE; note high degree of planar shear related foliation, ii) dyke, looking down, white arrows highlight quartz veins, iii) gneiss, note dominance of light areas and mm sized dark bands. (b) Shear zone centre; i) subvertical, planar dyke-gneiss contact (white dashed line) with dyke on right and gneiss on left; looking W. ii) Dyke, looking down, with vertical foliation and iii) & iv) abundance of variably sheared quartz veins in the dyke (white arrows).

but is more creamy white to light brown on a fresh surface and foliation is defined by mm-scale bands of quartz and plagioclase (Fig 3b i inset). Aligned elongate plagioclase clusters again define the deformed dyke fabric, the elongation of which varies in intensity on 10's cm- to m-scale, perpendicular to strike (Fig 3b ii). Multiple fabric-subparallel quartz veins up to 2 cm wide are present within the deformed dyke, some of which exhibit isoclinal folds with axial surfaces subparallel to the fabric (Fig 3b iii-iv).

4.2. Quantification of field shape fabric variation and quartz vein abundance in the dyke

Four strain maps, conducted along 10-15 m long transects perpendicular to the dyke, show a significant change in strain type and distribution at the outcrop scale, and quartz vein abundance, from $\sim$ 350 m away from the shear zone, to the shear zone centre (L3-6, Fig 1b; Fig 4). To quantify these changes we defined four strain types (T) based on the shape fabric of plagioclase aggregates identified in the field: (T0) background isotropic igneous texture with no preferred shape orientation, (T1) shape preferred orientation but no defined foliation, (T2) elongated plagioclase aggregates define $\geq$ 1 mm spaced foliation fabric and, (T3) $<$ 1 mm spaced foliation fabric (Fig 4a).

At 350 m from the shear zone centre (L3) the fabric in the dyke is dominated by (60 %) T0 lenses which are embedded in anastomosing, relatively narrow cm – 10's cm wide bands of predominantly T1 fabric. No quartz veins are observed. At 250 m from the shear zone centre (L4) the width of T1 bands is increased to $\sim$ 50 cm and the geometry is more planar. One foliation-parallel quartz vein is observed within a T1 band between unde-

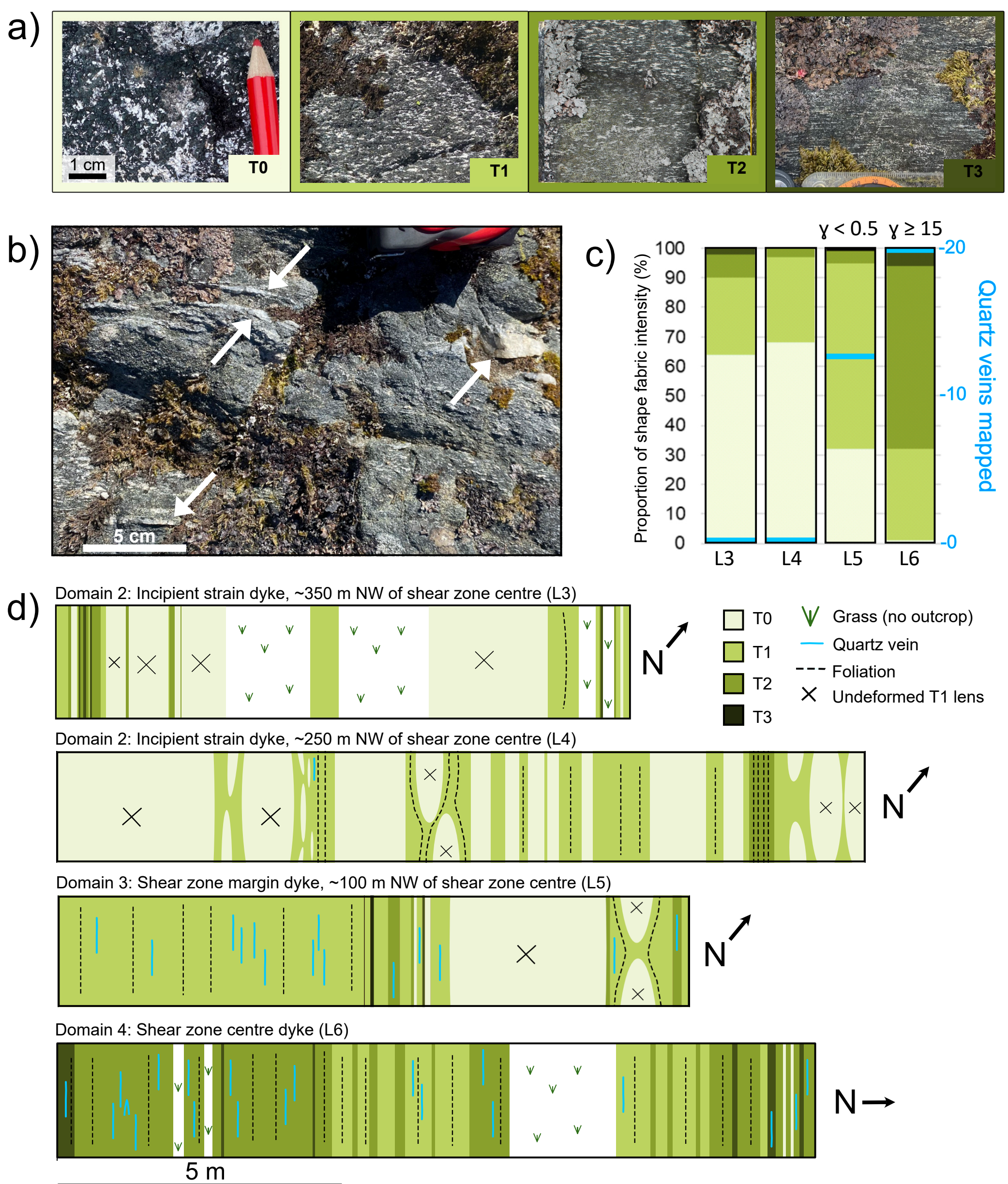

Figure 4: Field photos and maps, showing the field characterisation of dyke shape fabric types (T0-3) and structural domains 1-4. (a) Typical outcrop images of strain types (T) in dyke based on field shape fabric; note T number increases with increasing strain. (b) White arrows highlight cm-scale quartz veins in shear zone centre dyke T2. (c) Field shape fabric intensity and quartz vein abundance for each strain map shown in d), with strain estimates from Tatham and Casey (2007). T colours correspond to a) where light to dark green corresponds to low to high shape fabric. (d) Representation of measured strain maps along 10-15 m transects across dyke with decreasing distance to shear zone. See Figure 1b for locations (L3-6).

formed T0 lenses (Fig 2d i inset). 100 m from the shear zone centre (L5), 70 % of the strain map has T1 fabric, which is generally planar except for where it wraps around a couple of undeformed lenses. Across this transect 13 quartz veins are observed, 1-2 mm wide and up to 60 cm long. In the shear zone centre (L6) 100 % of the dyke exhibits T1 or higher planar fabric and 20 quartz veins, up to 2 cm wide and subparallel to fabric, are observed within the strain map.

To summarise, the percentage of deformed rock volume, and intensity of shape fabric, increases from 30 % deformed rock 350 m and 250 m from the shear zone centre, to 100 % deformed rock in the shear zone centre (Fig 4c). In addition, fabric-parallel or subparallel, 0.5-20 mm wide, up to 60 cm long quartz veins increase in abundance towards the shear zone (Fig 4c). In the two strain maps furthest from the shear zone centre T1, or in some cases T2, bands anastomose around lenses of T0 dyke, whereas closer to the shear zone the fabric becomes planar and more homogeneous (Fig 4d).

4.3. Structural domains

Based on the field strain fabric mapping and shear strain (γ) derived by Tatham and Casey (2007), we distinguish 4 structural domains to determine the change in structure and chemistry towards the shear zone (Fig 1b). Domain 1 'wall rock' represents the background rock where minimal deformation associated with the shear zone has occurred. Domain 2 'incipient strain' represents incipient shear, where localised bands of strain anastomose around undeformed lenses of rock. In Domain 3 'shear zone margin' $\geq$ 70 % of the rock is deformed and fabric is predominantly planar, oblique to the shear zone ($\gamma < 0.5$ according to Tatham and Casey 2007). In Domain 4 'shear zone centre' 100 % of the rock is deformed, and lineations and planar fabric are parallel to the shear zone ($\gamma \sim \geq 15$).

4.4. Microstructures and phase distribution and abundance

Here we present an overview of the microstructures, phase distribution and mineral chemistry observed in the dominant fabric type (dyke type T0-3; gneiss weak to strong) for the respective structural domain (Fig 1b). Table S1 in Supplementary data lists the samples used for analyses.

4.4.1. Domain 1 'wall rock'. Undeformed dyke and high grade foliated granulitic gneiss; dominant dyke fabric type T0

Dyke: The wall rock consists of 60 % amphibole, 30 % plagioclase, 5 % quartz and 1 % clinopyroxene, clinozoisite, titanite, ilmenite and apatite (Table 1). The texture is isotropic and correlates with T0 (Section 4.2; Fig 5a i). 1-3 mm clusters of either amphibole or plagioclase grains dominate, within which different grain populations are observed, determined by their grain size and mineralogy (Fig 5a i-iv). The plagioclase clusters consist of 60 % large ($\sim$ 0.3-0.8 mm) and 40 % small (< 0.3 mm) grains. Of the large plagioclase grains, $\sim$ 70 % appear light brown in colour due to extensive alteration to sericite and $\sim$ 30 % are colourless and minimally altered. The small plagioclase grains are generally colourless, minimally altered and exist between and at the margins of large plagioclase grains (Fig 5a ii-iv). Individual, large ($\sim$ 0.2-0.5 mm) amphibole grains form roughly 10 area% and exhibit a range of chemistry: 1) opaque ilmenite-speckled cores with rims which are replaced to varying degrees by clear green amphibole, 2) entirely clear green amphibole or 3) clear green amphibole with quartz $\pm$ clinopyroxene inclusions (Fig 5a

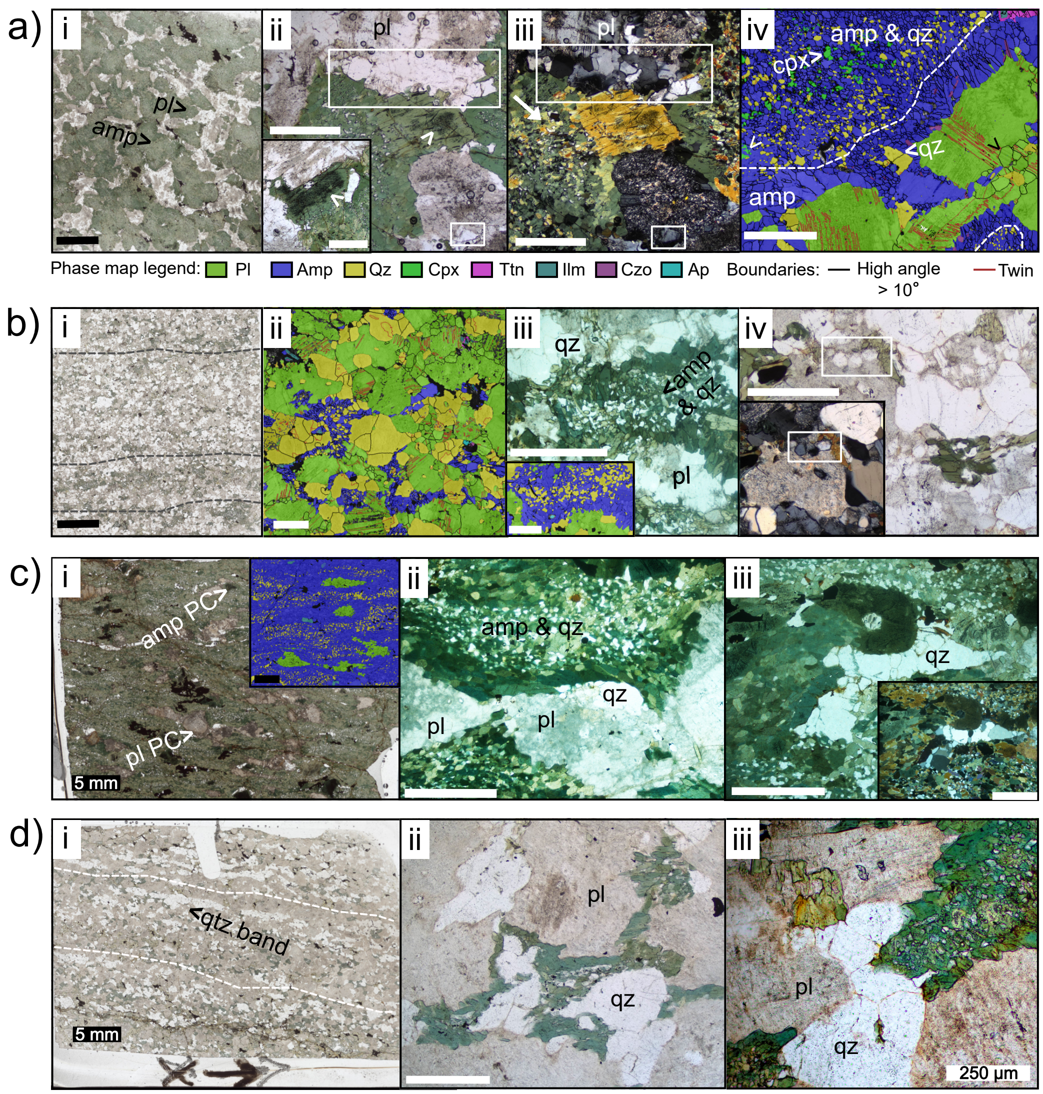

Figure 5: Optical microstructures of domain 1 'wall rock' and 2 'incipient strain' dyke (a & c) and gneiss (b & d), shown with thin section scans, photomicrographs in plane-polarised light (PPL) or cross-polarised light (XPL) where indicated, and EBSD false colour phase maps. Phase abbreviations after Whitney and Evans (2010). (a) Dyke, domain 1 T0 (AS2239); i) isotropic fabric, ii) amp cores (white arrow) with replacement front, iii) XPL version of (ii) showing unaltered small pl grains (white boxes) and iv) outline of parent cpx grains (dashed lines). (b) Gneiss, domain 1 (AS2240a); i) weak fabric (dashed lines), ii) & iii) phase distribution and iv) unaltered small pl grains (white boxes). (c) Dyke, domain 2 T1 (AS2153); i) & ii) elongate fabric and iii) qz beard preferentially grown in X direction with XPL inset. (d) Gneiss, domain 2 (AS2151); i) weak fabric (dashed lines) with discontinuous qz bands (black arrow) and ii) & iii) phase distribution. Black scale bar: 1 mm and white bar: 500 μm, unless stated otherwise.

ii-iv). Distinct areas of small (< 0.1 mm) intermixed amphibole and quartz, sometimes with remnant < 0.1 mm clinopyroxene in their centre, comprise 50 area% (Fig 5a ii-iv). At the boundary of plagioclase clusters and grains, a margin of medium size (0.1-0.2 mm) amphibole often exists, effectively separating plagioclase from amphibole-quartz $\pm$ clinopyroxene areas (Fig 5a iv). Individual large (0.1-0.2 mm) quartz grains are spatially associated with large plagioclase and amphibole (Fig 5a iv), all of which exhibit undulose extinction to some extent.

Gneiss: The gneiss wall rock consists of 55 % plagioclase, 30 % quartz, 10 % amphibole, 5 % chlorite and ≤ 1 % ilmenite, clinozoisite, titanite and apatite (Table 1). It has a weak fabric defined by lighter quartz-plagioclase bands and darker green amphibole-rich bands (Fig 5b i). Large plagioclase (0.2-1 mm), quartz (0.1-0.6 mm) and amphibole grains (0.1-0.4 mm) form roughly 60 area% (Fig 5b ii). Approximately 30 area% consists of distinct domains of smaller (<0.1 mm) intermixed amphibole-quartz, with a margin of medium sized amphibole grains where adjacent to plagioclase (Fig 5b iii). Of the large plagioclases, around 70 % are light brown where altered to sericite and 30 % are colourless and minimally altered (Fig 5b iii). Small ($<$ 0.2 mm), unaltered plagioclase grains exist between or at the boundaries of larger plagioclase grains and make up 10 area% (Fig 5b iv). Similar to in the dyke the large plagioclase, quartz and amphibole exhibit minor undulose extinction.

Table 1: Mineral proportion estimates from EBSD phase maps, EDX maps and thin sections. Domain numbers refer to domains: (1) wall rock, (2) incipient shear, (3) shear zone margin and (4) shear zone centre (see Fig 1b). Mineral abbreviations after Whitney and Evans (2010). Hydrous phases are listed in blue, late alteration phases are listed in orange.

Dyke sample	**Domain**	**Fabric type**	**Amp**	**Pl**	**Qz**	**Cpx**	**Czo**	**Ilm**	**Ttn**	**Ap**	**Chl**	**Ms**
AS2239	1	T0	**60**	30	5	1	**1**	1	1	0	0	0
AS2153	2	T1	**70**	20	10	0	**<1**	1	<1	0	0	0
AS2237*	3	T1	**70**	20	10							
AS2160	4	T2	**75**	15	10	0	**<1**	1	0	<1	0	0
AS2158	4	T3	**80**	5	10	0	**5**	1	0	<1	0	0
*no EBSD data												
Gneiss	**Domain**	**Strain**	**Pl**	**Qtz**	**Amp**	**Bt**	**Czo**	**Ilm**	**Ttn**	**Ap**	**Chl**	**Ms**
AS2240A	1	Low	55	30	**10**	**0**	**<1**	<1	<1	<1	5	0
AS2151	2	Low	55	30	**10**	**0**	**<1**	<1	<1	<1	5	0
AS2155	3	Medium	60	30	**5**	**5**	**1**	<1	0	<1	<1	<1
AS2157	4	High	60	30	**3**	**5**	**<1**	0	0	0	2	<1

4.4.2. *Domain 2 'incipient strain'. Low strain fabrics; dominant deformation dyke fabric type T0*

Dyke: Here 65-70 % of the dyke has no (T0) strain fabric and 30 % is comprised of low (T1) strain fabric (Fig 4). Compared to domain 1 T0, T1 strain fabric has increased amphibole and quartz (10 % and 5 % more respectively), 10 % less plagioclase and no clinopyroxene. It has a similar phase distribution to the dyke wall rock, however, grains and grain domains are now elongated to form a weak fabric and here large grains (amphibole and plagioclase) are evenly distributed throughout the smaller-grained matrix as porphyroclasts (Fig 5c i-ii). Plagioclase clusters, now comprised predominantly of small grains, show the beginnings of attenuation and disaggregation in the X direction. Amphibole grains which envelop plagioclase clusters are rotated to align in the X direction (Fig 5c ii). Large grained quartz beards form adjacent to plagioclase and amphibole porphyroclasts, having grown preferentially in the X direction (Fig 5c iii).

Gneiss: The gneiss mineralogy, grain populations and phase distribution are similar to the 'wall rock' domain 1, however here the fabric is more strongly defined by narrow, discontinuous quartz or amphibole bands within wider, continuous plagioclase bands (Fig 5d i). Similar to domain 1 dyke, amphibole grains adjacent to plagioclase are rotated to align in the X direction, and an overall shape preferred orientation is observed (Fig 5d ii-iii).

4.4.3. *Domain 3 'shear zone margin'. Heterogeneously deformed dyke and quartzofeldspathic gneiss; dominant dyke fabric type T1*

Dyke: The dyke is composed of 65 % T1 strain fabric and 30 % T0 (Fig 4). While domain 2 and domain 3 T1 strain fabric appear similar in outcrop

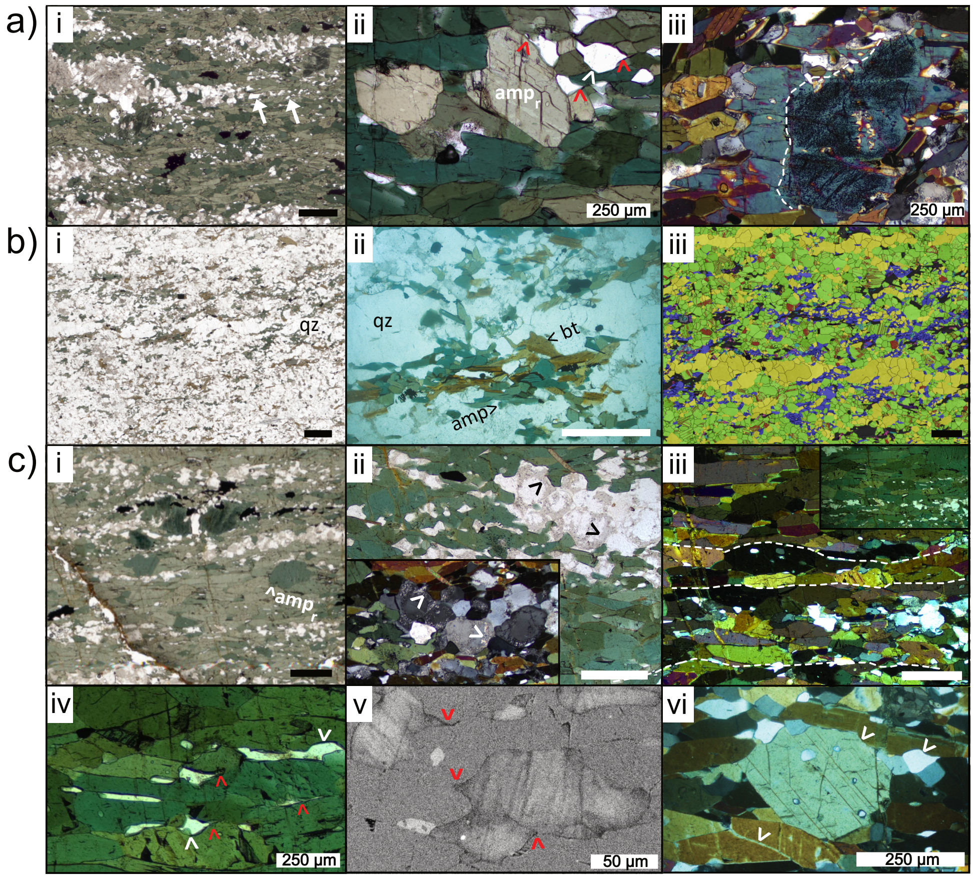

Figure 6: Optical microstructures of domain 3 and 4 dyke (a & c) and gneiss (b), shown with thin section scans, photomicrographs in plane-polarised light (PPL) or cross-polarised light (XPL) where indicated, and EBSD false colour phase maps (see Fig 5 for legend). (a) Dyke domain 3 T1 (AS2237); i) elongate pl clusters and disseminated qz (white arrows), ii) elongate amp (amp$_e$), more rounded, equant amp (amp$_r$), indentation (white arrows) and tails (red arrows), iii) XPL amp beard preferentially grown in X direction (dashed lines denotes replacement front). (b) Gneiss domain 3 (AS2155); i) semi-continuous qz band ii) bt association with amp, iii) pl-dominant matrix with large grains qz bands. (c) Dyke domain 4 T2 (AS2160); i) elongate pl bands with elongate amp matrix and more rounded, equant amp (amp$_r$), ii) heterogeneous pl seritisation, inset: XPL. iii) XPL planar surface along aligned amp (dashed lines), iv) qz indentation (white arrows) and tails (red arrows), v) CL image of qz showing darker tails preferentially grown in X direction (red arrows) and vi) photomicrograph showing amp-amp and amp-qz grain indentation (white arrows). Black scale bar: 1 mm and white bar: 500 μm, unless stated otherwise.

and share the same mineralogy, in the microstructure the phase distribution differs. Here, small-grained amphibole-quartz bands are not observed and instead intermediate grain size (0.1-0.3 mm) amphibole forms the matrix framework (Fig 6a i). This amphibole is elongate and strongly aligned in the X direction (amp_e, Fig 6a ii). A small number (~ 5 %) of amphibole grains are more equant, almost rounded and are oriented differently to amp_e (amp_r, Fig 6a ii). In addition, a number of ilmenite-speckled amphibole porphyroclasts remain, with a rim of clear amphibole grown preferentially in the X direction (Fig 6a iii). Small (< 0.1 mm) quartz is predominantly observed as individual grains around the tails of elongated plagioclase clusters, and as disaggregated bands within amphibole matrix (Fig 6a i). These individual quartz, and occasionally plagioclase, grains are often elongate with preferentially grown tails formed in the X direction, or exist as individual grains with high aspect ratios between elongate amphibole grains (Fig 6a ii). These grains are often seen to 'indent' amphibole grains (Fig 6a ii).

Gneiss: Compared to domains 1 and 2 gneiss, domain 3 gneiss comprises 5 % more plagioclase and 5 % less of both amphibole and chlorite (Table 1). Notably, 5 % biotite is observed, spatially associated with amphibole, and plagioclase is generally colourless with only < 5 % altered to sericite (Fig 6b i-ii). The large plagioclase and large individual quartz grains observed in domains 1 and 2 gneiss are not present here; instead small (0.2 mm) plagioclase dominates the matrix, interspersed with individual grains or discontinuous bands of 0.1 mm quartz $\pm$ amphibole and biotite, aligned in the X direction (Fig 6b iii). Occasional quartz bands, boudinaged and semi-continuous in the X-direction (Fig 6b iii), have a larger (~ 0.5 mm) grain size compared to the matrix and exhibit undulose extinction.

4.4.4. Domain 4 'shear zone centre'. Strongly and homogeneously deformed dyke, strongly deformed gneiss; main deformation dyke fabric T2

Dyke: Here the dyke is composed predominantly of T2 (60 %) and T1 (30 %) strain fabric and some T3 (7 %, Fig 4). Compared to T1, T2 dyke consists of 5 % more amphibole, 5 % less plagioclase and titanite is not present as an accessory mineral (Table 1). Grain populations and distribution is very similar to domain 3 T1, except that plagioclase clusters are elongated here into flattened and discontinuous bands rather than clusters, with a grain size of 0.1-0.5 mm (Fig 6c i). 40 % of the plagioclase is altered to sericite, with both altered and unaltered plagioclase intermixed within the plagioclase bands and individual grains (Fig 6c ii). Similar to domain 3, T1, intermediate (0.5 mm), elongate and aligned amp_e forms the matrix framework (Fig 6c i-ii). Amp_e often align to form continuous linked surfaces extending several grains in the X direction, with or without small < 0.15 mm individual quartz or plagioclase grains grown between aligned amp_e (Fig 6c iii). As in domain 3 T1, these small quartz and plagioclase are observed as disseminated bands in the amphibole matrix and at the margins of plagioclase clusters or amphibole porphyroclasts, as thin films between amp_e or elongate with tails preferentially grown in the X direction (Fig 6c iv-vi). In quartz these preferentially grown tails exhibit reduced CL-response compared to the overall grain (Fig 6c v). Quartz, plagioclase and amphibole grains themselves often 'indent' adjacent amphibole grains in the Z direction, perpendicular to foliation (Fig 6c iv & vi).

T3 mineralogy and phase distribution is distinct from T1-2; only 5 %

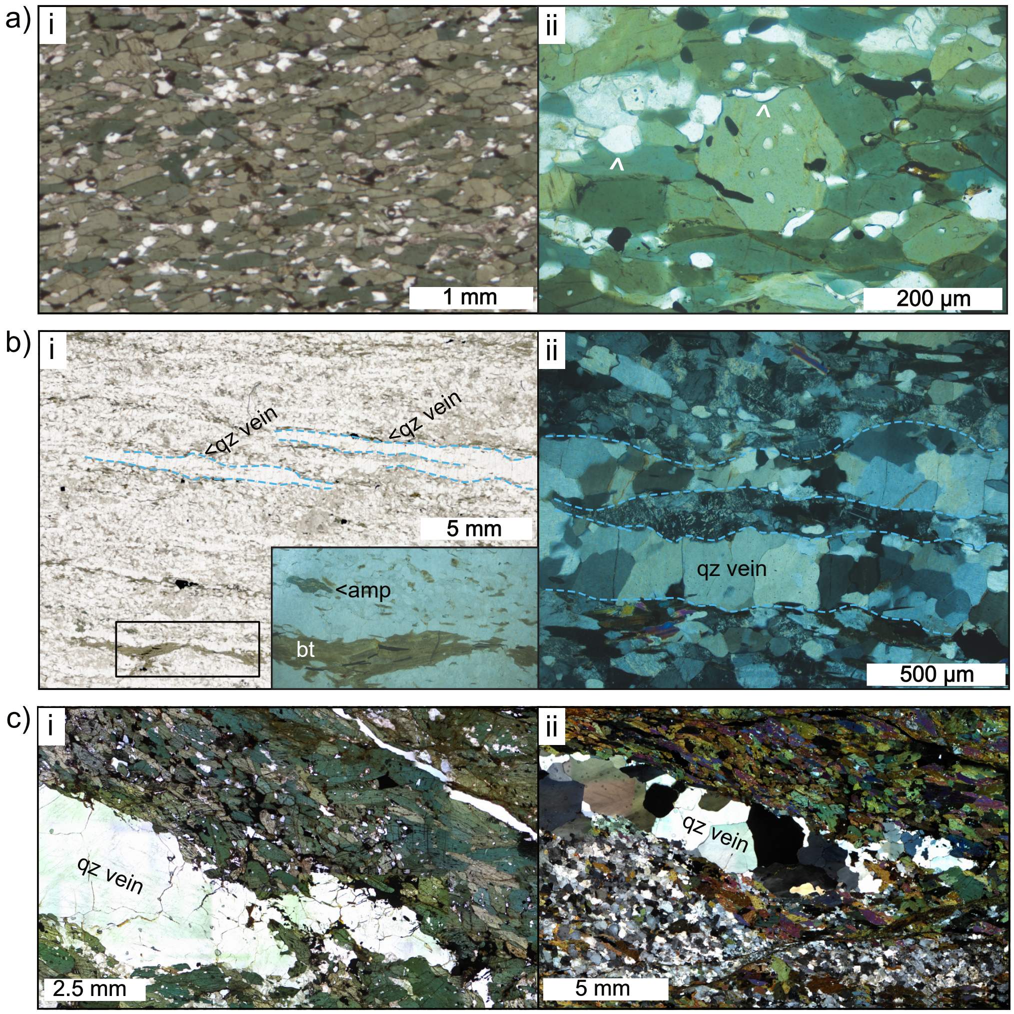

Figure 7: Optical microstructures of domain 4 high strain dyke (a) and gneiss (b), and a mm wide quartz vein in dyke (c & d), shown in photomicrographs in plane-polarised light (PPL) or cross-polarised light (XPL) where indicated. (a) Dyke domain 4 T3 (AS2158); i) qz, pl, ilm and czo are disseminated in amp matrix, ii) asymmetric qz distribution around rounded, equant amp (amp$_r$) within elongate amp (amp$_e$) matrix, grain indentation (white arrows) and preferentially grown tails (red arrows). (b) Gneiss domain 4 high strain (AS2157); i) fabric-parallel qz veins and bt seams, and ii) different populations of qz: large-grained vein and smaller grains in pl-dominant matrix. (c) Stitched photomicrograph of qz vein formed at local dyke-gneiss contact in i) PPL and ii) XPL.

plagioclase remains and 5 % clinozoisite is present, quartz, plagioclase, clinozoisite and ilmenite are entirely disaggregated within the 80 % amphibole matrix, and grain size is largely unimodal as very few to no original large grains remain (Fig 7a i). However, in common with domain 3 T1 and domain 4 T2 are specific microstructures such as indented grains, elongate, aligned tails and thin films, and aligned grain boundaries – despite the more uniform distribution of phases here (Fig 7a ii).

Gneiss: Adjacent to T3 dyke, the gneiss mineralogy is similar to domain 3, albeit with marginally less amphibole. Here the gneiss has a strong fabric defined by 2 mm wide plagioclase domains and subparallel, continuous quartz bands (Fig 7b i). Biotite forms semi-continuous layers, often adjacent to quartz veins and in places biotite is seen to replace amphibole (Fig 7b ii). Plagioclase has a grain size of 0.1-0.2 mm and is only lightly altered to sericite, while subparallel, cm-long quartz bands (likely quartz veins) comprise larger 0.2-0.4 mm grains (Fig 7b ii).

Quartz veins: In both the dyke and gneiss, where observed in thin section, quartz veins show a larger grain size compared to the surrounding matrix, of up to 2 mm and 0.5 mm respectively, and undulose extinction (Fig 7b ii & c ii). In the shear zone centre, quartz veins are rare at sample scale in the dyke, however, in the high strain gneiss we see numerous quartz veins close together. The quartz veins in the gneiss show a variety of straight or undulatory boundaries, and are often associated with biotite (Fig 7b i).

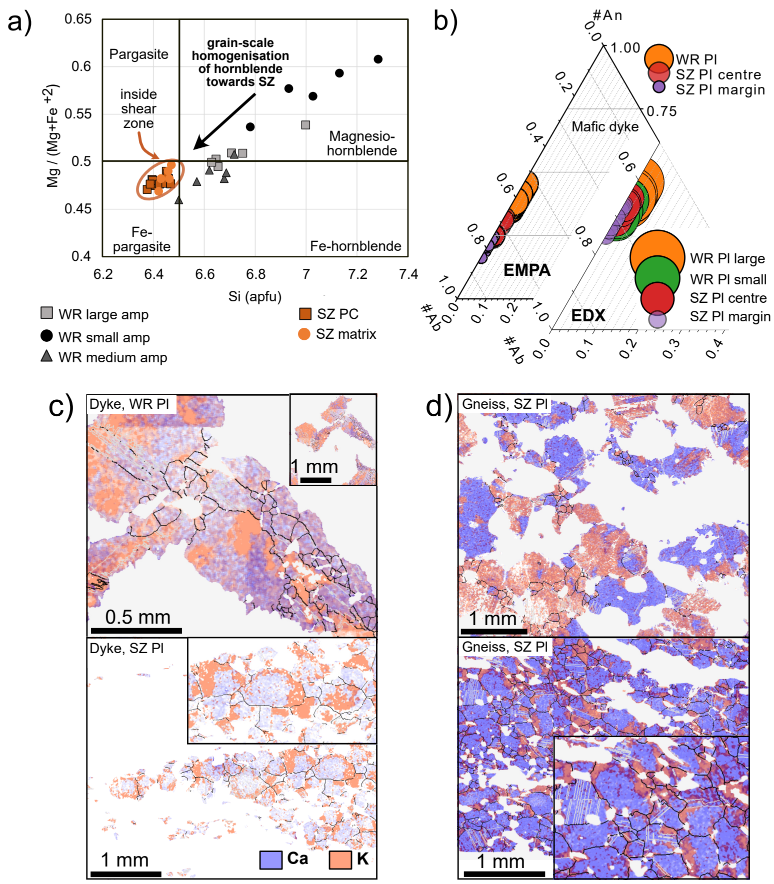

Figure 8: Amphibole and plagiocalse chemistry in dyke and gneiss. (a) EMPA data for amphibole in dyke wall rock and shear zone (small grains < 100 μm, medium grains 0.1-02 μm). Si vs Mg# plot after Leake et al. 1997. (b) EMPA and EDX data for plagioclase in dyke wall rock and shear zone centre (small grains < 300 μm). (c & d) EDX chemistry maps for dyke (c) and gneiss (d) show asymmetrical, structural control on K-rich seritisation in the shear zone centre where blue = Ca and orange = K. High angle grain boundaries in black and twin boundaries in red.

4.5. Changes in mineral chemistry

4.5.1. Dyke: Amphibole composition is varied in wall rock but homogeneous in shear zone

In the dyke wall rock a range of amphibole chemistry exists across the amphibole populations, with compositions trending between magnesio-hornblende (6.8-7.3 Si and 0.55-0.6 Mg#) and Fe-hornblende (6.5-6.7 Si and 0.45-0.5 Mg#, Fig 8a). In contrast, the shear zone amphibole has a homogeneous Fe-pargasite composition. Within the wall rock, the magnesio-hornblende population most distinct from the shear zone is the small (< 0.1 mm) amphibole observed in amphibole-quartz $\pm$ clinopyroxene areas (Fig 5a iv). The Fe-hornblende population, closest in composition to the shear zone, is the medium (0.1-0.2 mm) sized amphibole which forms a margin between plagioclase and amphibole-quartz $\pm$ clinopyroxene areas (Fig 5a iv). Between these two wall rock end-members is the clear green amphibole associated with large (0.2-0.5 mm) grains, which has an intermediate hornblende composition (Fig 8a).

4.5.2. Systematic change in plagioclase composition from wall rock to shear zone centre

In the dyke, where unaltered, large plagioclase have an andesine (0.5-0.7 #Al) composition while small plagioclase have a slightly higher albite content andesine-oligoclase composition (0.6-0.75 #Al, Fig 8b). In the shear zone centre, plagioclase is only lightly altered to sericite and overall has an andesine-oligoclase composition (0.65-0.85 #Al, Fig 8b). However, the centre and margin of individual grains exhibit distinct chemistry, with grain margins comprising a slightly higher albite content (0.75-0.85 #Al) compared to the centre of grains (0.65-0.8 #Al, Fig 8b). Figure 8c illustrates how the spatial distribution of alteration of plagioclase to K-rich sericite in the wall rock compares to alteration in the shear zone centre. In the wall rock, large plagioclase is variably altered to sericite with a generally even distribution of alteration within grains, while small plagioclase is generally unaltered. In the shear zone centre, alteration to sericite occurs primarily at the margin of grains, and preferentially in the long axis of aligned, elongate plagioclase grains (Fig 6c ii & Fig 8c). The gneiss exhibits a similar alteration pattern to the dyke, with large plagioclase variably altered to sericite and small plagioclase minimally altered in the wall rock, and sericite alteration observed primarily in the long axis of aligned, elongate plagioclase grains in the shear zone centre (Fig 8d).

4.6. Quantitative changes in grain size with increasing strain

4.6.1. Dyke: With increasing strain, grain size and phase abundance decreases in plagioclase and increases in quartz and amphibole

Overall, plagioclase median grain size decreases slightly with increasing proximity to the shear zone, from 50 μm in the wall rock to ~ 35 μm in the shear zone centre (Fig 9a). In contrast, quartz and amphibole median grain size increases with proximity to the shear zone, respectively from $\sim 30 \mu m$ and ~ 25 μm in the wall rock to ~ 40 μm and ~ 80 μm in the shear zone centre (Fig 9a). This evolution is illustrated in Figure 9b where small grains populations (amphibole < 80 μm, plagioclase < 300 μm and quartz < 100 μm) are highlighted as a subset to illustrate the different grain populations described in Section 4.4 and grain size is plotted in an area-weighted fraction histogram.

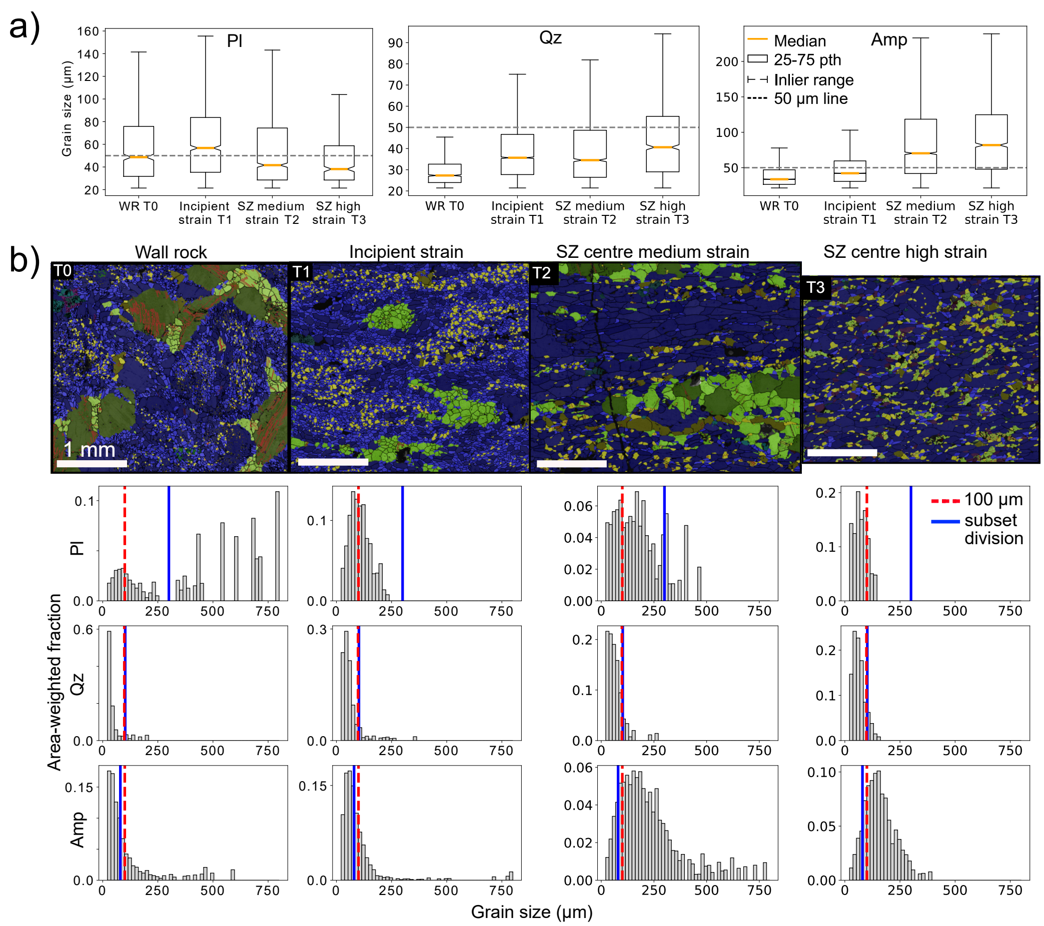

Figure 9: Dyke grain size change with increasing strain and proximity to shear zone. (a) Box and whisker plots for equivalent circle diameter grain size, with increasing strain and proximity to the shear zone. The whiskers extend to 1.5 times the interquartile range (IQR), and so do not display outlier data points. (b) EBSD false colour phase maps showing the grain size and phase distribution change associated with increasing strain (T0-3), and corresponding area-weighted grain size fraction histograms. Small grain populations (pl $< 300\ \mu m$, qz $< 100\ \mu m$, amp $< 80\ \mu m$) are highlighted in phase maps where amp = blue, pl = green and qz = yellow. Note increased phase mixing, homogenisation of grain size and fabric strength from left to right. Red line in histograms represents 100 μm, and blue line denotes the subset grain size threshold for each phase. White scale bar: 1 mm.

In domain 1 T0 grain size is bimodal with significant proportions of amphibole, plagioclase and quartz both above and below the subset threshold (Fig 9b). Small amphibole grains occur predominantly in amphibole-quartz $\pm$ clinopyroxene areas away from plagioclase, and $> 80\ \mu m$ amphibole is spatially associated with plagioclase. In domain 2 T1 fewer large grains are observed and plagioclase clusters are almost entirely small grains (Fig 9b). In domain 4 T2, few small amphibole grains exist and they generally exist alongside individual small quartz and plagioclase grains close to plagioclase clusters. Instead, bands of $> 80\ \mu m$ amphibole exist away from plagioclase clusters. In domain 4 T3 quartz and plagioclase are generally below the subset threshold, while amphibole is generally above (Fig 9b). Domain 4 amphibole and quartz grain size is generally unimodal, respectively above and below the subset threshold (Fig 9b). Plagioclase is bimodal in domain 4 T2 due to very small individual plagioclase grains in the amphibole matrix adjacent to plagioclase clusters (Fig 9b). In domain 4 T3, all plagioclase is now very small and disseminated within the amphibole matrix. Overall, domain 1 the area-weighted grain size distribution shows a large range but is dominated by small grains, however, with increasing strain the median area-weighted grain size increases and the range decreases, to produce a more unimodal distribution in domain 4 (Fig 9b).

4.6.2. Gneiss: In the shear zone grain size increases relative to wall rock

In the gneiss the grain size of plagioclase, quartz and amphibole (where present) is ~ 50 % greater in domains 3 and 4, compared to domain 1 (Fig 10a). The median grain size in domain 1 is $\sim$ 60, 35 and 350 μm for plagioclase, quartz and amphibole, respectively compared to $\sim$ 100, 70 and 60 μm

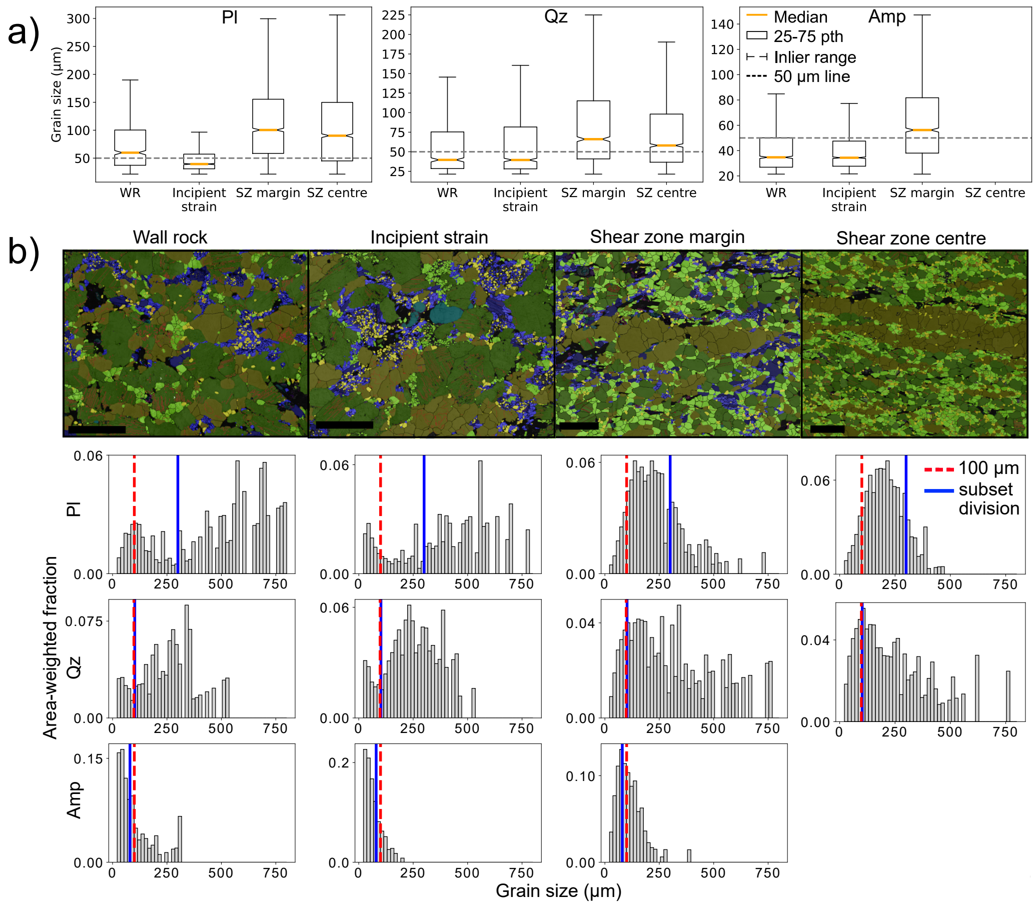

Figure 10: Gneiss grain size change with increasing strain and proximity to shear zone. (a) Box and whisker plots for equivalent circle diameter grain size, with increasing strain and proximity to the shear zone. The whiskers extend to 1.5 times the interquartile range (IQR), and so do not display outlier data points. (b) EBSD false colour phase maps showing the grain size and phase distribution change associated with increasing strain, and corresponding area-weighted grain size fraction histograms. Small grain populations (pl < 200 μm, qz < 100 μm, amp < 120 μm) are highlighted in phase maps where pl = green, qz = yellow and amp = blue. Note increased phase mixing, homogenisation of grain size and fabric strength from left to right. Red line in histograms represents 100 μm, and blue line denotes the subset grain size threshold for each phase. Black scale bar: 1 mm.

respectively in domains 3 and 4.

In Figure 10b small grains (amphibole < 120 μm, plagioclase < 200 μm and quartz < 100 μm) are highlighted as a subset to illustrate the different grain populations described in Section 4.4. Like in the dyke, domains 1 and 2 have a bimodal grain size with large, original grains and small reacted or recrystallized grains (Fig 10b). Domains 3 and 4 matrix grain size is more unimodal, with plagioclase and amphibole grain size distribution almost entirely below 400 μm, however, quartz is an exception (Fig 10b). Quartz veins that are $\sim$ 1 mm wide and continuous over cm's have a larger grain size between 200-800 μm (Fig 10b). Discontinuous quartz bands that are < 0.5 mm wide and < 1 cm in length have a grain size intermediate between small (< 100 μm) quartz disseminated within the plagioclase matrix and the quartz vein large grains.

4.7. Changes in crystallographic orientation and shape fabric with increasing strain

4.7.1. Dyke

In dyke domain 1 T0 none of the main phases (amphibole, plagioclase, quartz) show any significant overall SPO or CPO (Fig 11a). The aspect ratio of amphibole (large and small) and large plagioclase grains is 2.5 and 2.45, respectively. Quartz (large and small) and small plagioclase grains have an aspect ratio of 1.75 and 1.8, respectively. In domain 4 T2 and T3, whilst plagioclase and quartz still show no overall CPO, amphibole has a strong CPO with the c-axis [001] aligned in the X-direction, and the a-axis [100] parallel to the Z-direction, and all three main phases (quartz, plagioclase, amphibole) show a significant SPO with their long axes aligned in the X-

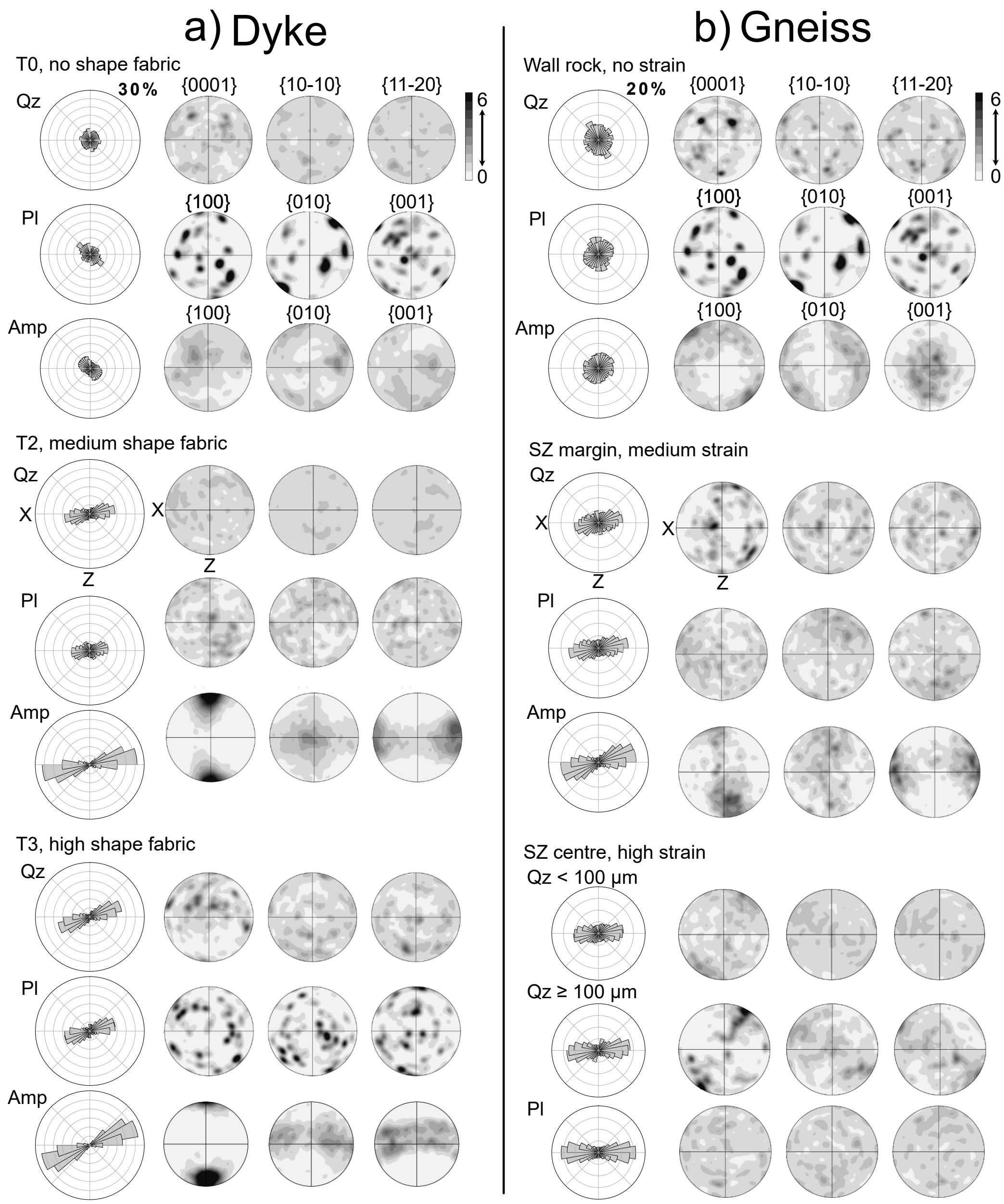

Figure 11: Shape and crystallographic orientation data for the main phases (qz, pl and amp) showing microstructure change with increasing strain and proximity to shear zone in (a) dyke and (b) gneiss. Rose graphs display fitted ellipse angle as a proxy for shape-orientation and pole figures plot crystallographic-orientation. The shape fabric type (T0-3, dyke; low-high, gneiss) for each sample is shown. Dyke and gneiss SPO increases in all 3 phases with increasing strain and proximity to shear zone, but only amp develops a CPO with the exception of high strain gneiss where 'large' qz $\geq$ 100 μm also shows a CPO. Pole figure colour bars show multiples of uniform density (MUD) values with a range of 0-6, oriented data is shown in the XZ plane.

direction (Fig 11a). The aspect ratio of amphibole, plagioclase and quartz is greater here compared to domain 1, with aspect ratios of 2.85, 2.5 and 2, respectively, in domain 4 T2. Note that the SPO is strongest in these phases in the higher strain domain 4 T3, compared to domain 4 T2.

Although there is no overall CPO in domain 1 T0, locally, the intergrown, small grained amphibole-quartz $\pm$ clinopyroxene areas (Fig 5a iv) exhibit for each area an area specific CPO with a clear crystallographic relationship to the parent clinopyroxene such that the amphibole CPO is the same as the parent clinopyroxene (Fig 12a). In addition, the amphibole fringe formed between amphibole-quartz $\pm$ clinopyroxene areas and plagioclase locally exhibits a CPO that corresponds with the amphibole-quartz $\pm$ clinopyroxene area to which it is adjacent (Fig 12a). Large grain populations (amphibole: 0.2-0.5 mm, plagioclase: 0.3-0.8 mm and quartz: 0.1-0.2 mm) exhibit significant, crystallographically-controlled intra-grain orientation change (7-8°), while small and medium grains (small amphibole and quartz < 0.1 mm, medium amphibole: 0.1-0.2 mm and small plagioclase < 0.3 mm) exhibit little to no ($\leq 1°$) intra-grain orientation change (Fig 12b).

In domain 4 T2, neither the elongate matrix amphibole (0.1-0.3 mm) nor plagioclase (0.1-0.4 mm) show significant internal deformation ($< 2°$ within a single grain), however, remnant, large amphibole grains (1 mm) are randomly oriented compared to the amphibole matrix and possess 12° orientation change (Fig 12c), similar to those in Domain 1 T0. In domain 4 T3, none of the main phases show any significant internal deformation, and large grains are absent (Fig 12d).

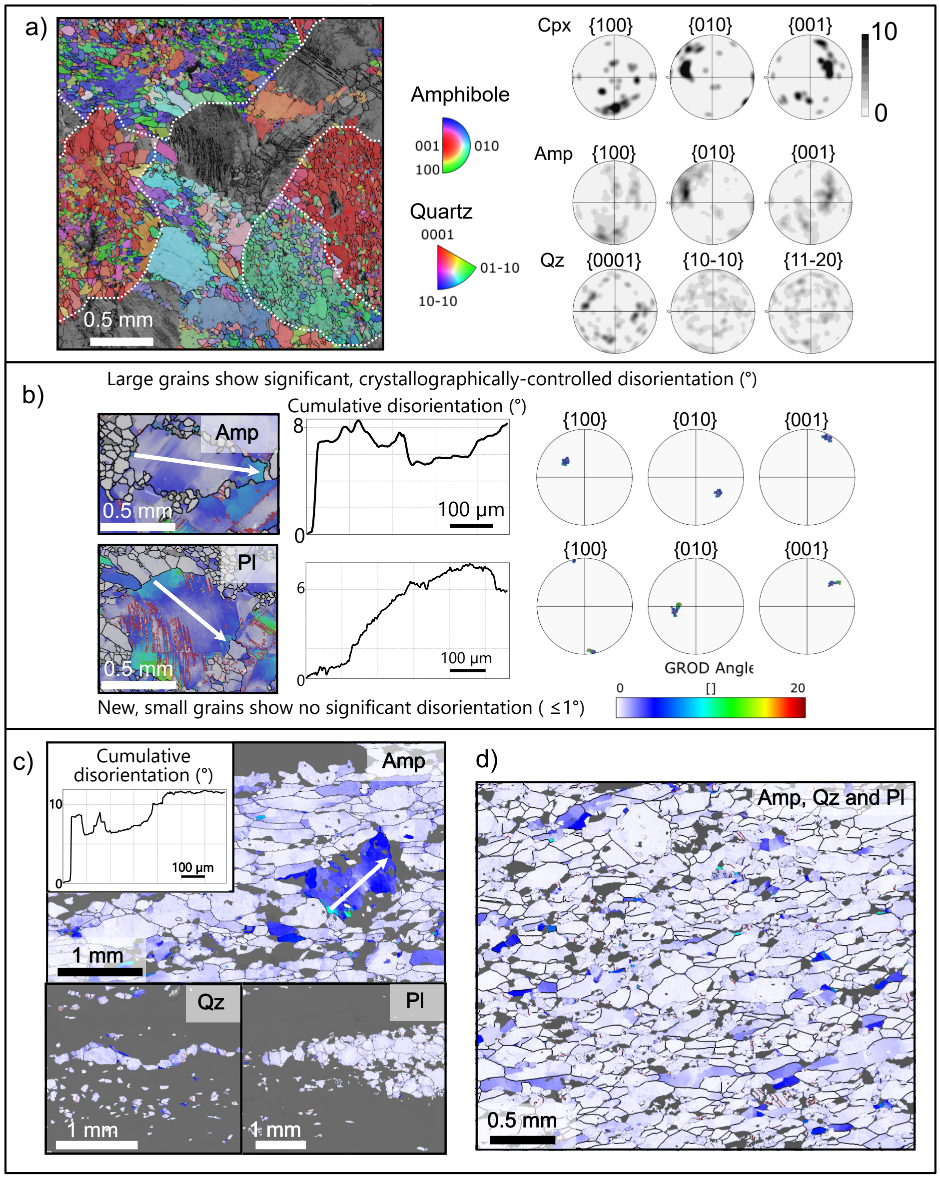

Figure 12: Dyke: Crystallographic-orientation data and maps showing local, reaction-controlled CPO in wall rock amphibole and grain size-control on grain relative orientation deviation (GROD) i.e. intra-grain deformation. Maps are underlain by BSE maps. (a) Domain 1 T0 (AS2239); inverse pole figure (IPF) map of amp shows local, area-specific orientation which correlates with area-specific pole figures that show local area-specific orientation of amp is related to parent cpx grain. Pole figure colour bars show multiples of uniform density (MUD) values with a range of 0-10. (b) Domain 1 T0 (AS2239); GROD maps and cumulative disorientation measurements show i) 7-8° crystallographically-controlled internal deformation of large grains and $<1°$ internal deformation of small, new grains. (c) Domain 4 T2 (AS2160); small, new grains show $\leq 2°$ internal deformation while large remnant amp shows $> 10°$ internal deformation. (d) Domain 4 T3; GROD map shows little to no internal grain deformation in amp, qz and pl.

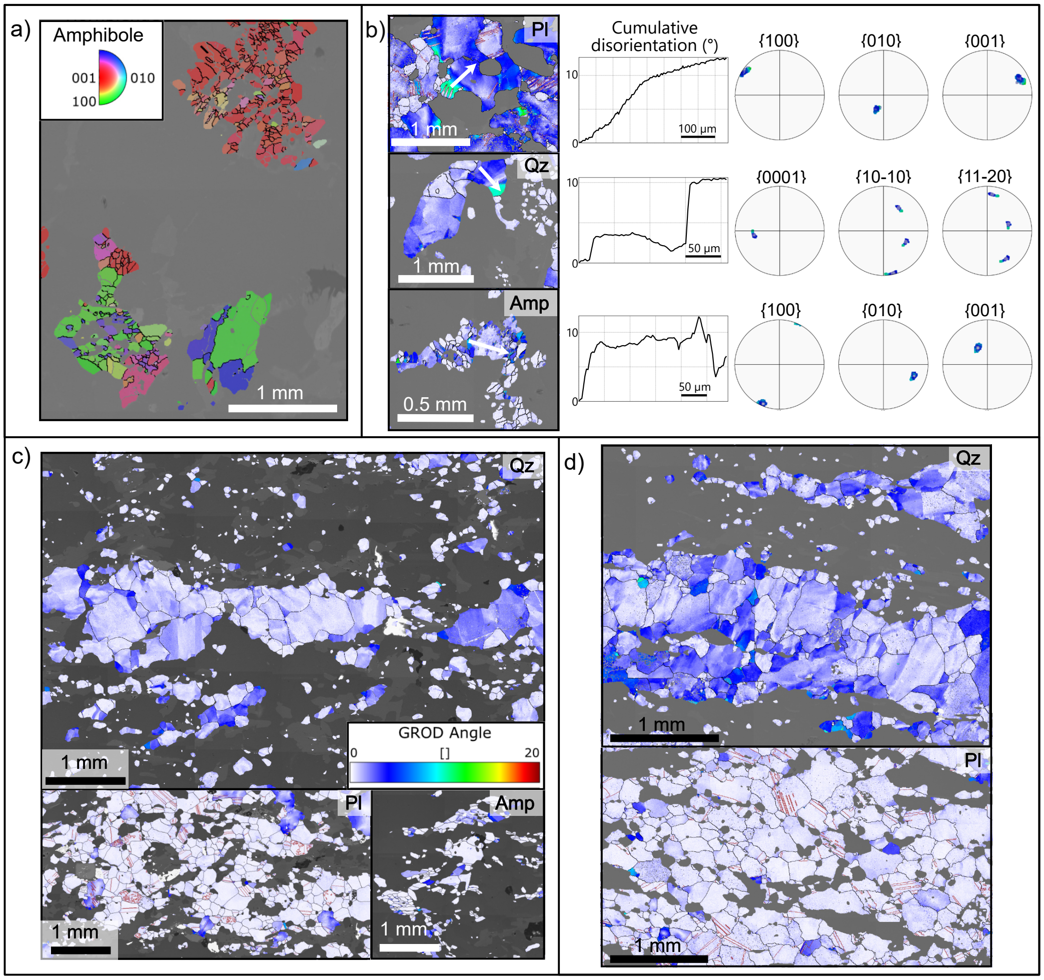

Figure 13: Gneiss: Crystallographic-orientation data and maps showing local, reaction-controlled CPO in wall rock amphibole and grain size-control on grain relative orientation deviation (GROD) i.e. intra-grain deformation. Maps are underlain by BSE maps. (a) Domain 1 wall rock (AS2240a); inverse pole figure (IPF) map of amp shows local area-specific orientation. (b) Domain 1 wall rock (AS2240a); GROD maps and cumulative disorientation measurements show i) 10-13° of crystallographically-controlled internal deformation in large grains and $< 2°$ of internal deformation in small, new grains. (c) Domain 3 medium strain (AS2155); GROD maps show minimal internal deformation of pl, amp and small qz, but up to 8° internal deformation in large qz. (d) Domain 4 high strain (AS2157); GROD map shows little to no internal deformation in pl and small qz, but up to 8° internal deformation in large qz.

4.7.2. Gneiss

Similar to dyke domain 1 T0, in the gneiss domain 1, none of the major phases (plagioclase, quartz, amphibole) show any significant overall SPO or CPO (Fig 11b). The aspect ratio of (large and small) amphibole, plagioclase and quartz is 2, 1.8 and 1.65, respectively. In domain 3, whilst plagioclase and quartz still show no overall CPO, amphibole has a CPO with the c-axis [001] aligned in the X-direction, and the a-axis [100] parallel to the Z-direction, and all three main phases (quartz, plagioclase, amphibole) show a significant SPO with their long axes aligned in the X-direction (Fig 11b). In domain 4, plagioclase has an even stronger SPO but still no CPO, amphibole is absent and quartz has a stronger SPO in grains $\geq 100\ \mu m$, together with a CPO showing a rotated c-axis [0001] girdle (Fig 11b). Quartz grains $< 100\ \mu m$ show a very faint rotated c-axis girdle. There is a slight increase in the aspect ratio of plagioclase and quartz in domain 4, compared to domain 1, with aspect ratios of 1.9 and 1.7, respectively.

In domain 1, again similar to dyke domain 1, the intergrown small grained amphibole-quartz areas (Fig 5b) often exhibit locally an area specific CPO (Fig 13a). Of the different grain size populations in T0, the large grain populations (plagioclase: 0.2-1 mm, quartz: 0.1-0.6 mm and amphibole: 0.1-0.4 mm) exhibit significant and systematic orientation change within individual grains (up to 14°, Fig 13b). This corresponds to the undulose extinction observed optically (Section 4.4). In contrast, small grains (plagioclase: $<$ 0.2 mm, quartz: $<$ 0.1 mm and amphibole: $<$ 0.1 mm) exhibit little to no orientation change within individual grains.

In domain 3, neither amphibole ($<$ 0.2 mm), plagioclase (0.1-0.4 mm), nor small quartz (< 0.15 mm) show significant internal deformation ($< 2°$ within a single grain), however, semi-continuous bands of large (0.3-0.8 mm) quartz possess up to 8° intragranular orientation change (Fig 13c). Domain 4 plagioclase and quartz show similar internal deformation signatures, but with more pervasive large quartz intra-grain deformation (Fig 13d).

5. Discussion

5.1. The development of Badcall shear zone in a metastable granulite-facies terrane at mid-crustal amphibolite-facies conditions: Reactions, phase changes and fluid influx

Mineralogy within the shear zone is fully equilibrated to amphibolite-facies conditions (pargasite + andesine-oligoclase), in both the dyke and gneiss. This is in agreement with estimated P-T conditions: 510–660°C and 5–8 kbar/500-800 MPa (Beach, 1973; Sills, 1982; Cartwright, 1990; Droop et al., 1999; Pearce and Wheeler, 2014). In the wall rock, chemically and/or microstructurally distinct grain populations delineate different reactions in space and time. To determine the relative timing of these populations, in this section we follow their evolution towards the shear zone centre where the most advanced hydration reactions occur.

In the dyke wall rock, the small ($< 100\ \mu m$) amphibole in amphibole-quartz ± clinopyroxene areas (amp_{cpx} and qz_{cpx}) has the most distinct chemical composition with respect to the shear zone (Fig 5a i; magnesio-hornblende, Fig 8a). Amp_{cpx} show no significant internal deformation ($< 2°$) within individual grains, and discrete amp_{cpx}-qz_{cpx} ± clinopyroxene areas largely preserve the crystallographic orientation of the ≥ 1 mm parent clinopyroxene grain (Fig 12a). These grains are the direct result of static clinopyroxene hydration at amphibolite-facies conditions, driving topotactic replacement of clinopyroxene by amphibole (e.g. Shannon and Rossi, 1964; McNamara et al., 2012; Lee et al., 2022). As outlined by Beach (1980), this replacement reaction can also produce quartz, giving the general reaction:

$$\text{cpx} + \text{hydrous fluid} \rightarrow \text{amp}_{\text{cpx}} + \text{qz}_{\text{cpx}} + \text{hydrous fluid} \qquad \text{(reaction 1)}$$

The presence of clinopyroxene, predominately in the centre of some amp_{cpx}-qz_{cpx} areas, shows that hydration is only partial and is localised even at the mm-scale. At the margin of amp_{cpx}-qz_{cpx} areas, occasional larger (> 200 μm) amp_{cpx} grains contain qz_{cpx} $\pm$ clinopyroxene inclusions (Fig 5a iv) and bear an orientation which corresponds to that of adjacent amp_{cpx}-qz_{cpx} $\pm$ clinopyroxene areas (Fig 12a).

Large (> 200 μm) amphibole exhibit a range of chemistry: end-members exhibit either dark ilmenite-speckled cores with clear green rims, or entirely clear green grains, and between these end-members, grains show partial replacement of ilmenite-cores with clear green amphibole (Fig 5a ii-iii). We consider the ilmenite-speckled amphibole to be igneous (amp_0) which was originally a high temperature Ti-rich amphibole that exsolved Ti to form ilmenite during cooling (e.g. Mongkoltip and Ashworth, 1983). We consider these the result of static interface coupled replacement / dissolution-precipitation reactions (Putnis, 2009), which replaces the original igneous amphibole (amp_0) with new amphibole (amp_1).

We did not obtain chemistry for amp_0 because of the ilmenite inclusions, however, the chemistry of amp_1 (hornblende) is intermediate between

amp_{cpx} (magnesio-hornblende) and the chemistry of the medium-sized (100 – 200 μm) amphibole population which has the closest chemistry to the shear zone (Fe-pargasite, Fig 8a), and which we define as amp_2 (Fe-hornblende, Fig 8a). Amp_2 forms a reaction fringe between plagioclase and amp_{cpx}-qz_{cpx} $\pm$ clinopyroxene areas (Fig 5a iv). Similar to amp_1, amp_2 exhibits no crystal-plastic deformation features (i.e. no significant intra-grain lattice distortions). Similar to amp_{cpx}, amp_2 bears a crystallographic orientation similar to its remnant parent clinopyroxene, and appears to consume plagioclase where they are in contact (Fig 5a iv). Plagioclase chemistry changes during recrystallization from large original grains (pl_1) to small new grains (pl_2, Fig 5a i-ii; bimodal grain size, Fig 9b). Smaller grains are less altered by sericite and are higher in albite content (Fig 8b EDX). This chemical change during recrystallisation may accompany reaction with amphibole according to reaction 2:

$$\mathrm{amp} + \mathrm{pl}_{1,2} + \text{hydrous fluid} \rightarrow \mathrm{amp} + \mathrm{pl}_2 + \text{hydrous fluid} \qquad \text{(reaction 2)}$$

The gneiss wall rock comprises amphibole and plagioclase populations which are microstructurally analogous to amp_{cpx}, amp_1 and amp_2, with the same spatial and crystallographic relationships seen in the dyke, albeit with a lower amphibole content overall (10 modal % compared to 60 modal % in dyke wall rock, Table 1; Fig 5b i-iii; Fig 11b; Fig 13a). Given the uniform clear green appearance of amphibole in the gneiss wall rock, it is likely all amphibole here is metamorphic, having re-equilibrated to amphibolite-facies conditions. The observed chlorite is texturally late in the gneiss and related to static alteration unrelated to amphibolite-facies shear zone deformation and metamorphism (Table 1; reaction 6 in Beach 1980).

Both reaction 1 and reaction 2 require fluid input and evidence influx of fluid prior to significant deformation. While some grains show internal deformation (see Section 5.3 below), the preservation of local orientation of amp_{cpx}-qz_{cpx} areas and amp_2 reaction fringes evidences the lack of significant strain in the wall rock. Next we outline the evolution of grain populations and phase abundance towards the shear zone centre, which correspond with an increase in strain and hydration.

Grain populations similar to those in T0 dyke (Fig 5c & d) exist in T1 dyke and low-medium strain gneiss, however, here distinct areas of grain populations are elongate parallel to lineation. In T1 dyke, reaction 1 is complete and no clinopyroxene remains (Table 1), which means fluid is no longer absorbed during reaction 1 and fluid can instead facilitate deformation. The presence of quartz beards grown preferentially in the X-direction evidences precipitation of material from fluid (Fig 5c iii). In dyke T1, clusters of pl_2 are enveloped and partially consumed by preferentially aligned amp_2 and (clinopyroxene-absent) amp_{cpx}-qz_{cpx} areas exist in elongate bands away from pl_2 clusters (Fig 5c i inset & ii). The consumption of plagioclase to produce amphibole explains the 10-20 modal % increase in amphibole and decrease in plagioclase in deformed dyke, relative to the undeformed wall rock (Table 1). Overall, plagioclase clusters reduce in both grain size and cluster size through reaction-driven grain-size-reduction of original large grains to new, smaller and higher albite content grains, and the consumption of plagioclase to produce amphibole associated with reaction 2.

In domains 3 and 4 (shear zone margin and shear zone centre), amp_{cpx}-

qz_{cpx} bands are absent in dyke T1 and T2, and the spatial distribution of phases is significantly changed. Here, preferentially aligned, elongate amphibole forms continuous bands away from plagioclase clusters, and quartz and smaller amphibole exists predominantly in the tails of plagioclase clusters or large amphibole porphyroclasts (Fig 5a i & c i-ii). Mineral chemistry shows that matrix amphibole in the shear zone is entirely distinct from amphibole populations in wall rock T0 (Fig 8a). We interpret shear zone amphibole chemistry to form from a continuation of reactions 1 and 2, observed in domains 1 and 2 (wall rock and incipient strain), where amphiboles (amp_0, amp_{cpx}, amp_1 and amp_2) and plagioclase react with fluids infiltrating the rock to produce amp_{SZ}. Through this process, amp_{SZ} replaces earlier amphiboles due to their differing composition and/or non-optimal orientation. Amp_0 porphyroclast cores remain in places, however, clear green growth rims and beards bear the same chemistry as the matrix amp_{SZ} (Fe-pargasite). That wall rock amphibole populations trend towards amp_{SZ}, but that amp_{SZ} remains chemically distinct (Fig 8a), shows that this chemistry change occurs in a fluid-buffered system.

Plagioclase chemistry is also distinct in the shear zone, compared to the wall rock dyke T0. Plagioclase in the shear zone centre exhibits a higher albite content, particularly at grain margins (Fig 8b), and EDX maps show how the distribution of sericite alteration is structurally controlled, as alteration occurs predominantly in the long axis of grains grown preferentially in the X-direction (Fig 8c & d). Given the microstructural similarities between dyke T1 and T2 in domains 3 and 4, we propose that amphibole and plagioclase chemistry in shear zone centre is comparable to that in the shear zone margin. In domain 3 and 4 gneiss, a 5 % loss of amphibole and a 5 % increase biotite compared to domain 1 (Fig 6b; Fig 7b; Table 1) shows again the change in chemistry conditions and increased hydration:

$$\mathrm{ilm + amp + hydrous\ fluid \rightarrow bt + hydrous\ fluid} \qquad \text{(reaction 3)}$$

Overall, dyke wall rock amphibole populations are consumed and replaced by chemically distinct amphibole in the shear zone (amp$_{SZ}$, Fig 8a), where plagioclase exhibits a higher albite content and a chemical composition that is distinct in the long axis of grains aligned in the X-direction (Fig 8b-d). The absence of clinopyroxene in domains 2-4 and presence of biotite (in gneiss) and increased clinozoisite (in dyke) in domains 3 and 4 (Table 1) indicates a correlation between hydration, reactions and strain, as detailed previously by (Beach, 1980), and requires the introduction of external fluid.

5.2. Fluid influx: quartz vein abundance coincides with increase in hydration and strain towards shear zone

Tatham and Casey (2007) established a macro-fabric strain gradient from < 1 to 15 across the shear zone, based on the rotation of macro fabrics in the gneiss (Fig 1b). Our maps of shape fabric intensity at outcrop scale (Fig 4d) show heterogeneous distribution of strain in the dyke where discrete, anastomosing bands of T1 envelop undeformed T0 lenses, even in domain 2 where the dyke remains undeformed at map-scale (Fig 1b; Fig 2c i & d i-ii; Fig 4). From domain 2 to domain 4, strain in the dyke becomes more pervasive and homogeneously distributed. In domain 3 planar T1 fabric dominates > 60 % of the dyke and only limited T0 lenses exist (Fig 3a i & b ii; Fig 4). In domain 4 > 95 % of the dyke exhibits a planar fabric, with 60 % of the shape fabric comprised of higher strain T2 (Fig 4). The presence of remnant clinopyroxene in only T0 (Fig 5a iv) means hydration is incomplete in T0 dyke. In domains 2-4 T1-3, no clinopyroxene remains and hydration reaction 1 is complete, and the highest degree of hydration is found in domain 4 (biotite and clinozoisite present in gneiss and dyke respectively). Increased shape fabric intensity with increasing proximity of the shear zone is therefore correlated with increased hydration and strain.

The presence of hydrated mineral assemblage and increased shape fabric intensity is also correlated with the increased abundance of syntectonic quartz veins with increasing proximity to the shear zone (Fig 4 b-d). In the dyke, all but one quartz vein are observed in either the shear zone margin or shear zone centre (domains 3 and 4), and all quartz veins are observed within shape fabric T1-3 (i.e. not observed in T0). Due to the similarity in grain habit between a dyke quartz vein (Fig 7c) and quartz bands in gneiss domains 3 and 4 (Fig 6b; Fig 7b), we consider semi-continuous to continuous coarse quartz bands in the gneiss to represent deformed quartz veins. This suggests quartz veins are significantly more abundant in the gneiss, because a number of these deformed veins are present within individual thin sections (Fig 6b iii; Fig 7b). We consider the presence of these quartz veins to reflect the increase in fluid presence towards the shear zone.

Given the above, we consider hydration to increase from partial hydration in domains 1 and 2, where T0 dyke is relatively abundant, to effectively complete hydration in domain 4 where T0 dyke is near-absent. Hydration and degree of strain are correlated in space, with heterogeneous strain (and hydration) in domain 2, compared to strain (and hydration) that is more homogeneous in domain 3 and relatively uniform in domain 4. Spatial coincidence of hydration, strain and quartz vein abundance calls for causal relationships. The correlation of hydration and strain suggests deformation associated with the shear zone is facilitated by fluid. Quartz veins are known to be related to fluid influx (Sibson, 1981, 1994; Bons et al., 2012), and syntectonic quartz-carbonate veins have been previously reported in the nearby Gairloch shear zone (Beach, 1980). While the volume and source of fluid remains undetermined, the fact that we observe syntectonic quartz veins is proof of both fractures and localised fluid (Fig 3; Fig 4; Fig 7b & c). The source of the quartz may be internal and/or external: in part derived from fluid and/or derived entirely from the host rocks (i.e. Williams and Fagereng, 2022). It is important to stress that the quartz veins we observe here are small, discrete and discontinuous, relative to extensive quartz vein networks typically observed at shallower depths. Previous authors have proposed the introduction of fluids to the mid-crust during earthquakes, i.e. 'seismic pumping' proposed by Sibson (1981, 1994), and mid-crustal quartz veins have been found to bear an isotopic signature which indicates meteoric-fluid (McCaig, 1988; Stenvall et al., 2020). Other potential sources of shear zone fluid are magmatic or metamorphic.

5.3. *Remnant signatures of dislocation creep in metastable wall rock contrasts dominance of dissolution-precipitation creep signatures formed during amphibolite-facies conditions within shear zone*

5.3.1. *Wall rock records dislocation creep at high grade and limited amphibolite-facies hydration reactions*

In the wall rock there is no overall CPO or SPO (Fig 11), however, large ($\sim$ 1 mm) pl_1, amp_0 and amp_1 and ($>$ 0.1 mm) qz_1 grains in gneiss and dyke preserve signatures of crystal-plastic dislocation creep deformation accumulated by strain in the wall rock (dyke, Fig 12b; gneiss, Fig 13b). These include undulose extinction, crystallographic-controlled internal deformation of grains, and limited amp_1 subgrains. We know that the wall rock did not experienced any significant deformation since reactions 1 and 2 occurred because amp_{cpx} and amp_2 retain local area-specific CPO (dyke, Fig 12a; gneiss, Fig 13a), and the distribution of large and small plagioclase grains is not structurally controlled. However, because hydration reactions have occurred in the wall rock (Section 5.1), we know that the hydration associated with the shear zone extends further from the shear zone than does significant deformation. Therefore, hydration likely preceded the deformation associated with the shear zone in domains 2-4.

5.3.2. *Evidence for dissolution-precipitation creep as the dominant deformation mechanism within the shear zone*

Despite the development of SPO in all major phases and CPO in amphibole with strain (Fig 11), neither the deformed dyke nor gneiss exhibit signs of crystal-plasticity within individual grains (with the exception of large quartz in the gneiss, and remnant porphyroclasts in the dyke; Fig 12c & d;

Fig 13c & d). The development of SPO without significant internal deformation of grains is consistent with numerical models that produce grain shape change during grain-size-sensitive deformation processes that involve the movement of material from a surface of relatively high stress to a surface of lower stress. This can occur by strictly diffusive processes (Gardner and Wheeler, 2021), or by dissolution-precipitation creep where material is dissolved at surfaces of high stress, transported in grain boundary fluid and subsequently precipitated in areas of low stress (Malvoisin and Baumgartner, 2021). The development of SPO in the absence of internal grain deformation is consistent with field, microstructural and experimental studies which attribute deformation to dissolution-precipitation creep (Wintsch and Yi, 2002; Díaz Aspiroz et al., 2007; Stokes et al., 2012; Marti et al., 2018; Lee et al., 2022). Rare, large amphibole grains do show some internal deformation (Fig 12c), however, we consider these grains to represent amp_0 or amp_1 grains which have survived from pre-hydration deformation, or to have experienced elevated stress due to their larger grain size, which necessitates deformation by dislocation creep.

Additionally, development of CPO in amphibole in both dyke and gneiss without significant internal deformation of grains indicates that CPO formed by means other than dislocation creep. Kamb (1959) observes anisotropic grains growth, where 'the preferred orientation is that which minimizes the chemical potential required for equilibrium across the plane normal to the greatest principal pressure axis. Thus, the weakest axis of a crystal (e.g. c-axis of calcite) tends to align with the greatest principal pressure axis, or axes, while the strongest axis (e.g. c-axis of quartz) tends to align perpendicular thereto'. Preferential growth in the long axis of amphibole (an elastically anisotropic mineral) creates CPO in favourably orientated grains, accompanied by associated rigid body rotation through the dissolution (or truncation) of surfaces of unfavourable crystallographic-orientation and precipitation on favourably oriented grain surfaces (Fig 6c vi). Similar signatures have been identified where pre-existing chemical zoning in grains is preferentially truncated by dissolution as a fabric is formed during deformation (Wintsch and Yi, 2002; Stokes et al., 2012; Wassmann and Stöckhert, 2013; Moore et al., 2024). This aids the alignment of grain boundaries in the X-direction, creating planar surfaces which extend across several grains (Fig 6c iii), and look very similar to weak 'sliding' surfaces produced during numerical modelling of diffusion processes (Gardner and Wheeler, 2021). In this way, a microstructure favourable for co-operative grain boundary sliding develops. Semi-continuous aligned biotite seams in gneiss domains 3 and 4 (Fig 7b i) may behave similarly. The lack of CPO development in plagioclase and, in the dyke, quartz, is consistent with deformation by dissolution-precipitation creep because plagioclase and quartz are not significantly anisotropic minerals and as such they are not expected to produce a CPO in the same way as amphibole. In contrast, SPO does not rely solely on crystallographic control and therefore all three main phases develop a SPO that appears to reflect their anisotropy to some degree; in order of highest mineral anisotropy to least anisotropy, aspect ratios are 2.85, 2.5 and 2 in dyke T2 amphibole, plagioclase and quartz, respectively.

The progressive replacement of amp_0 by amp_1 from grain edge to grain centre in all four domains is a distinct signature of coupled dissolution-precipitation. Reactions in dyke domain 1 T0 occur statically and there is no structural control on the dissolution-precipitation interface (Fig 5a ii-iii). However, with increased strain in T1-3, amp_1 forms beards preferentially grown in the X-direction (Fig 6a iii), suggesting material is transported from the high stress surface (Z-direction) to the low stress surface (X-direction, i.e. Wintsch and Yi 2002). The homogeneous amphibole chemistry in dyke domain 4 T2, compared to the range in chemistry observed in dyke domain 1 T0, suggests that dissolution-precipitation processes have replaced grains entirely – no zoning is preserved except for infrequent amp_0 porphyroclast cores (Fig 8a). Similarly, the structurally-controlled plagioclase chemistry in domain 4 dyke and gneiss suggests mobilisation of material with preferential precipitation/growth in long axes aligned in the X-direction (Fig 8c & d), as does chemically distinct, preferentially aligned quartz tails in dyke domain 4 T2 (Fig 6c v). Similar asymmetric chemical zonation has been identified as a feature of dissolution-precipitation creep or diffusion creep processes in a number of studies (Wintsch and Yi, 2002; Stokes et al., 2012; Wassmann and Stöckhert, 2013; McNamara et al., 2024; Wintsch et al., 2024). The microstructure of individual quartz grains amongst amphibole matrix in dyke domains 3 and 4 suggests quartz indents (dissolves) amphibole in the Z-direction, while simultaneously developing thin tails in the X-direction (Fig 6a ii & c iv-vi). Thin quartz films between aligned amphibole grains are also very distinctive features, likely formed through the transport and precipitation of material along grain boundaries.

5.3.3. Minor component of dislocation creep inside the shear zone: grain size dependent strain partitioning allows wall rock signatures to survive

In both the dyke and gneiss, some component of dislocation creep is preserved inside the shear zone, despite the dominance of dissolution-precipitation creep signatures. In the dyke, internal deformation of large porphyroclasts is similar in magnitude to those in the wall rock ($> 10°$ cumulative disorientation), while the surrounding shear zone matrix has little to no internal deformation (Fig 12c & d). We interpret this as grain size strain partitioning: grain-size-sensitive dissolution-precipitation creep is most effective at small grain sizes and therefore the fastest strain rates occur within the smaller grain matrix, while larger porphyroclasts are less affected. In addition, the large grain porphyroclasts are often poorly aligned crystallographically, so rates of dissolution and precipitation will be less effective. Therefore, similar to the way in which preservation of large porphyroclasts is expected if grain-size-sensitive grain boundary sliding accommodated by dislocation creep or dislocation glide (DisGBS) is active (Warren and Hirth, 2006), here large porphyroclasts of amphibole are preserved as smaller matrix grains are weaker and therefore deform at lower stresses – producing some grain size strain partitioning. In domain 3 and 4 gneiss, larger grained quartz bands exhibit some internal deformation (Fig 13c & d), which could again reflect grain size partitioning of strain, or a rheological contrast between the surrounding plagioclase matrix and the quartz bands at the temperature of deformation. A weaker surrounding matrix would exert higher stress on the quartz bands, enabling deformation by dislocation creep.

To summarise, we consider the partial hydration and signatures of minor crystal-plastic dislocation creep observed in relatively undeformed dyke T0 to indicate volumes of rock that are fluid under-saturated and relatively strong. Towards the shear zone centre, greater degree of hydration allows for the activity of dissolution-precipitation creep and associated weakening of the rock. The limited presence of T1 in domain 2 dyke, which anastomoses around elongate lenses of T0, illustrates the heterogeneous and limited distribution of hydration and activity of dissolution-precipitation creep outside of the shear zone (Fig 4d). In domain 3, the m-wide regions of planar T1 dyke fabric suggest that hydration and the activity of dissolution-precipitation creep is much more pervasive in the shear zone margin. Finally, in domain 4 where planar fabric and strain is homogeneously distributed, we find that the entire shear zone centre is sufficiently hydrated, weak and able to deform pervasively by dissolution-precipitation creep.

5.4. Proposed shear zone model: Strain localisation of the metastable anhydrous crust by activation of dissolution-precipitation creep through failure-induced local hydration

5.4.1. Stage 0: Strong, anhydrous crust deformed in dislocation creep regime

Prior to shear zone initiation, granulite-facies, anhydrous, pyroxene bearing-quartzofeldspathic (TTG) gneisses form during the Badcallian tectonometamorphic event c. 2800 Ma (Sutton and Watson 1950; Park 1970, previously known as 'Scourian' granulites, Sutton and Watson 1950; Chapman and Moorbath 1977; Hamilton et al. 1979. A dolerite dyke (plagioclase, clinopyroxene, amphibole and minor quartz), part of the Scourie dyke swarm, intrudes under conditions of 450–500 °C and 500–700 MPa, 2400-1900 Ma (Tarney, 1963) between the Inverian and Laxfordian tectonometamorphic

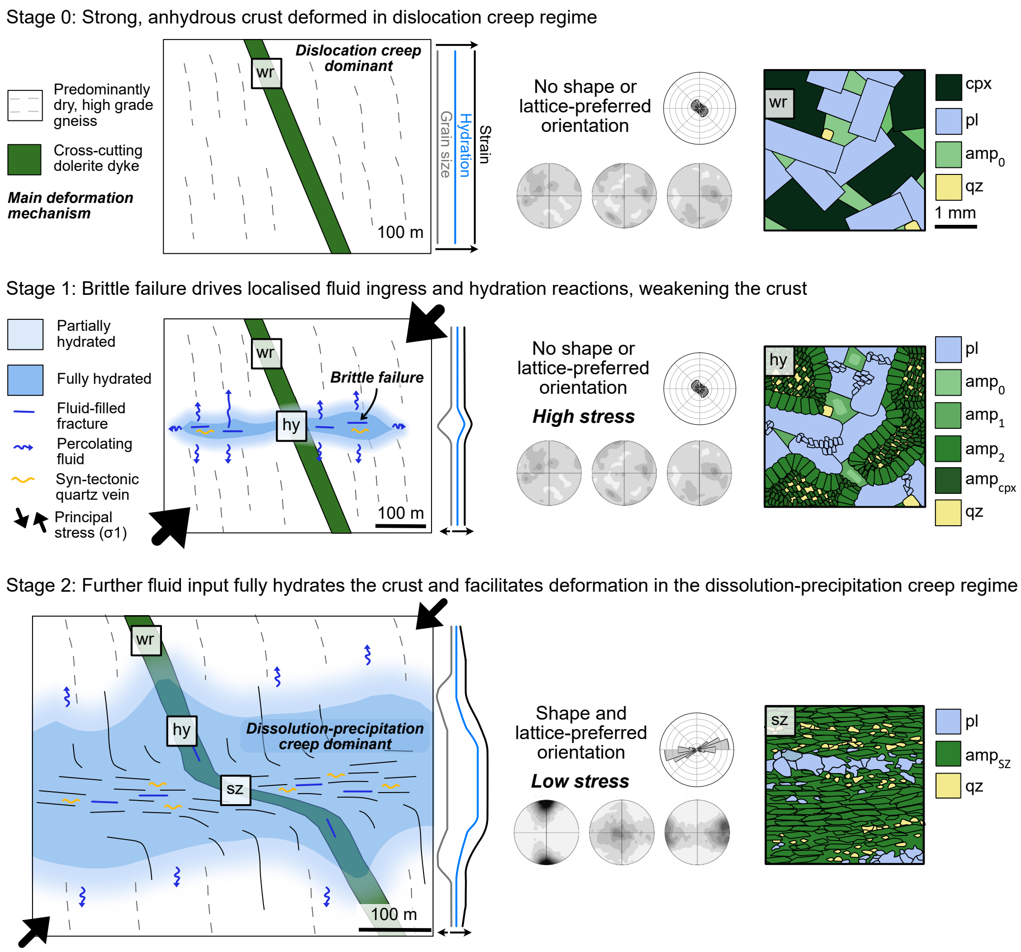

Figure 14: Schematic model of the evolution of the shear zone and associated microstructural development in the dyke; left, middle and right figures show schematically changes on the map scale, in SPO and CPO of main minerals and microstrutural features, respectively; note in italic dominant reaction and deformation processes; see text for further details. Stage 0: Strong, anhydrous crust deformed in dislocation creep regime. Stage 1: Brittle failure drives localised fluid ingress and hydration reactions, weakening the crust. Stage 2: Further fluid input fully hydrates the crust and facilitates deformation in the dissolution-precipitation creep regime. Spatial dissipation of fluid along grain boundaries and subsequent reaction of dry wall rock widens the zone of hydrated and weak rock over time, while the fluid activity decreases. Subsequent brittle failure and fluid ingress events allow the shear zone to mature to the 100-m-wide structure that we observe today.

events (Sutton and Watson, 1950; Park and Tarney, 1987). Far-field Laxfordian stress produces minor, dislocation creep regime, deformation in the coarse 1 mm grain size anhydrous gneiss and dyke, producing internal grain deformation and few subgrains (Section 4.7; Fig 5a & b; Fig 12b; Fig 13b). However, the preservation of original igneous, isotropic dyke T0 microstructure indicates very minor strain overall (Stage 0, Fig 14).

5.4.2. Stage 1: Brittle failure drives localised fluid ingress and hydration reactions, weakening the crust.

A high strain rate event (such as an earthquake) in the upper-crust extends into the mid-crust brittle-ductile transition zone and, where the relatively homogeneous crust fails in a brittle manner, introduces fluid into fractures (Stage 1, Fig 14). Where fluid is introduced to anhydrous crust bearing clinopyroxene, it will permeate along grain boundaries to drive initial hydration reaction 1 ($cpx + hydrousfluid \rightarrow amp_{cpx} + qtz_{cpx} + hydrousfluid$), weakening the rock through significant reduction in grain size of amphibole and quartz from 1 mm to $< 100\ \mu m$ (Fig 5a iv; wall rock, Fig 9; Stage 1, Fig 14). Where reaction 1 is incomplete and remnant clinopyroxene remains, continued reaction will consume, and limit the availability of, fluid such that sufficient fluid is not available to initiate dissolution-precipitation creep. Where reaction 1 is complete (clinopyroxene is entirely consumed), and grain boundaries are sufficiently wetted with freely available fluid, these areas begin to deform by dissolution-precipitation creep, switching the dominant deformation regime to from dislocation creep to dissolution-precipitation creep (Section 5.3). Strain subsequently localises in these areas because deformation in the dissolution-precipitation creep regime requires significantly less stress compared to dislocation creep, at equivalent P-T conditions. In this way, where hydration is complete and sufficient fluid is uniformly available the distribution of strain will be homogeneous. Where hydration is only local and partial, the distribution of strain will be heterogeneous.

5.4.3. Stage 2: Further fluid input fully hydrates the crust and facilitates deformation in the dissolution-precipitation creep regime.

New fluid is not required for deformation to continue in centre of the shear zone provided the grain boundaries stay wetted. However, grain boundary fluid may deplete through the process of free water consumption via hydration reactions in the surrounding anhydrous wall rock (e.g. Moore et al., 2020). If this depletion results in a lack of sufficient fluid along the grain boundaries, deformation will cease and shear zone will 'harden'. In contrast, if deformation by dissolution-precipitation creep starts a feedback where ongoing deformation allows drawing in of more fluid, then availability of fluid in the shear zone will increase and facilitate shear zone widening (Fusseis et al., 2009; Menegon et al., 2015). Is it possible that quartz only precipitates as veins where the rock is fluid-saturated? This could explain why quartz veins are only observed in completely hydrated rock (where no clinopyroxene remains), and are apparently absent in undeformed T0 areas bearing clinopyroxene (Fig 4c & d).

The finite width of shear zone suggests that a finite reservoir of fluid was available. Externally introduced fluid would likely dissipate with time, producing a transient effect. Repeated fracture and fluid infiltration events allow the hydrated region of shear zone to widen, with fluid permeating out and reacting with the surrounding wall rock ahead of the deformation zone as the shear zone evolves (Stage 2, Fig 14; i.e. Moore et al. 2020, 2024). To summarise, local fluid influx triggers activation of low stress dissolution-precipitation creep and localised strain. This process offers a mechanism for rheological transients in the mid-crust, as identified in geophysical data (Ingleby and Wright, 2017; Hussain et al., 2018; Weiss et al., 2019; Tian et al., 2020). Further work is needed to fully understand how these transient processes align with our existing geologically-derived flow laws, and with geophysical observations of transient deformation processes.

5.5. Wider rheological implications

5.5.1. Similar bulk strain rates in quartzofeldspathic gneisses and mafic dykes contrast local differences at the grain scale

That both the gneiss and dyke exhibit the same planar fabric and lineation in domains 3 and 4 (Fig 2a), and that the dyke-gneiss contact is planar (Fig 3b i), suggests both lithologies have a similar bulk rheology. The absence of undulatory fabric or pinch and swell structures at the contact between the two lithologies implies there is no significant rheological contrast (Fig 3b i), which would create boudinage or an undulatory fabric (Gardner et al., 2017b). This means for dissolution-precipitation creep, the gneiss and dyke behave very similarly. These field observations agree somewhat with laboratory experiments which find that amphibolite, deformed with 1 wt% water, and anorthite exhibit a similar rheology at wet, lower-crustal conditions (Getsinger et al., 2013; Getsinger and Hirth, 2014). In their amphibolite experiment, clinopyroxene is replaced with amphibole, and so we suggest metamorphic reactions in the presence of fluid during deformation is a similar, if not the same process as dissolution-precipitation creep, in which material is dissolved into grain boundary fluid, transported and precipitated at a new site – the location of which is dependant on the stress field. A previous study of Lewisian Gneiss Complex amphibolite-facies metamorphism and deformation concludes that the mafic dykes are weaker than the surrounding gneisses, based on pre-deformation metamorphic reactions that reduce grain size (Pearce et al., 2011). During early deformation of the Upper Badcall shear zone it is possible that this holds true, as the overall grain size is larger in the gneiss than the dyke in domains 1 and 2 (Figs 9b i-ii & 10b i-ii). However, once the shear zone and deformation fabrics are evolved (i.e. domains 3 and 4) then the grain size is similar for both the gneiss and the dyke and this could explain their apparently similar rheology (Figs 9b i-ii & 10b i-ii). At the microscale we see that plagioclase clusters in the dyke are not boudinaged once they have been thinned into bands with a similar grain size to the amphibole matrix in domains 3 and 4 (Fig 6c i; Fig 9b iii). This again suggests that, at the microscale, amphibole and plagioclase have a similar rheology in this deformation regime.

5.5.2. Localised activation of 'Newtonian' dissolution-precipitation creep as a trigger for strain localisation – a special case or not?

In the absence of other factors, Newtonian behaviour alone cannot localise deformation. Hence, for such a process to be important in the localisation of strain then additional processes must occur. As outlined above, we suggest that a local introduction and availability of fluid determines where strain localises through the activation of deformation by dissolution-precipitation creep, which is weaker than dislocation creep. Existing literature attributes strain localisation to dissolution-precipitation creep in a number of cm- to m-scale mid-crustal shear zones (Menegon et al., 2008; Giuntoli et al., 2018; Lee et al., 2022; Moore et al., 2020, 2024); however, our study is a rare recognition of dissolution-precipitation creep in a large 100-m-scale shear zone. This poses a number of questions: why are observations of this process in shear zones rare, and how important is dissolution-precipitation creep as a deformation mechanism in the mid-crust? Moore et al. (2020) suggests fluid influx triggers metamorphic differentiation and shear localisation. Is this a general feature or singular?

It is pertinent to consider whether signatures of dissolution-precipitation creep have been largely misinterpreted as annealed in some scenarios, due to the subtle signatures it produces in rocks: a lack of intra-grain deformation (crystal-plasticity) and relatively large grain size relative to typical mylonites produced by dynamic grain size reduction. The non-genetic definition of such deformed rocks would be blastomylonites: cohesive, foliated fault rocks with pronounced grain growth (Sibson, 1977; Woodcock and Mort, 2008); however, this definition means blastomylonites are invariably associated with annealing processes. In our study, the nature of matrix formation in the shear zone is by grain size refinement (grain size reduction or increase depending on the starting grain size and chemistry), and overall grain size increase in the dyke (amphibole and quartz) and gneiss (Figs 9 & 10). Grain size increase is in this case consistent with numerical models that demonstrate grain growth with deformation (Bons and Den Brok, 2000; Piazolo et al., 2002) and observations from elsewhere in the Lewisian Gneiss Complex (Beach, 1974a; Pearce et al., 2011). We suggest it is possible that significant deformation by dissolution-precipitation creep in the mid- to lower-crust has been overlooked as a signature of post-deformational annealing in some scenarios, and may be more common than currently thought. Related to the potential misinterpretation of the signatures produced in rocks by dissolution-precipitation creep is the fact that dissolution-precipitation creep can produce CPO in elastically anisotropic minerals such as amphiboles and phyllosilicates (Kamb, 1959; Bons and Den Brok, 2000; Wenk et al., 2020). This means that areas of the crust interpreted to deform by dislocation creep based on their seismic anisotropy, may in fact deform by dissolution-precipitation creep if a significant proportion of anisotropic minerals are present.

Finally, this process offers a mechanism that can produce transient rheology in the mid-crust, as a response to discrete fluid input weakening followed by a gradual strengthening through dissipation of that fluid through reaction and spatial migration. Further work is needed to understand how this transient fluid-reaction-deformation cycle influences large-scale deformation of the continental crust, and to align geological knowledge of flow laws with geophysical observations and models. Laboratory experiments that can capture the process of dissolution-precipitation creep across a range of lithology, deformation and P-T conditions would greatly aid the implementation of this process into rheological models.

6. Conclusions

In this study we outlined how the localised introduction of fluid facilitates the localisation of strain through the activation of dissolution-precipitation creep in a 100-m-wide mid-crustal shear zone. Our results demonstrate that dissolution-precipitation creep can be a significant process in the mid-crust, if enough fluid is available for grain boundaries to be sufficiently wet. We propose a model for shear zone evolution that follows a delocalising process: the zone of hydration extends beyond the zone of active deformation, which in turn allows the zone of deformation to widen. The presence of this fluid is likely to be a transient process, resulting in the short-term activation of dissolution-precipitation creep within a shear zone, until the available fluid has been taken up by the surrounding host rock. We propose a model for shear zone evolution in which there is an interplay between several related processes: (1) the localisation of strain controlled by the spatially-limited influx of fluids initially infiltrating through small-scale brittle cracking at the brittle-ductile transition, (2) the switch from a dislocation creep regime to dissolution-precipitation creep where sufficient fluid is available, (3) the progressive widening of the deformation zone, as hydration gradually extends beyond the zone of active deformation, (4) the homogenisation of microstructures and grain-chemistry through dissolution-precipitation creep within the shear zone, and (5) the removal of rheological differences resulting from small-scale mineralogical variability (particularly between plagioclase and amphibole). Exactly how these various processes interact, and control the life cycle of the shear zone, remains uncertain.

Signatures of dissolution-precipitation creep identified in the Upper Badcall shear zone include strong CPO development of amphibole contrasted by weak to absent CPO for quartz and plagioclase, and strong SPO in amphibole, plagioclase and quartz develops in the absence of significant crystal-plasticity. In addition, we observe indented, asymmetrically truncated, and flattened grains, and preferentially grown chemically distinct beards and elongate tails, and within amphibole or biotite-dominant areas, grain boundaries align to form planar surfaces extending several grains, potentially as 'weak sliding surfaces'. That grain size increases from outside the shear zone to inside the shear zone does not require annealing: instead the interplay between deformation and grain growth through anisotropic dissolution and precipitation in the shear zone promotes a relatively homogeneous microstructure inside the shear zone. Plagioclase and amphibole rocks can behave similarly when deforming by dissolution-precipitation creep, which agrees with laboratory experiments that deform both wet anorthite and amphibolite.

We suggest signatures of dissolution-precipitation creep may be overlooked in the mid- to lower-crust, which has a number of consequences in our understanding of how the Earth's crust deforms. Seismic anisotropy can be the result of deformation by dissolution-precipitation creep as well as dislocation creep, and the transient response of the mid- and lower-crust through the seismic cycle could be in part the result of the mobilisation of fluids during earthquakes, which drives a switch in the dominant deformation mechanism. In future, the identification of rheological signatures of dissolution-precipitation creep may be possible in other shear zones, whilst at the same time, there is the potential for the signature of dissolution-precipitation creep to be recognised in transient process in geophysical data - either through seismological studies of shear zone structure, or geodetic studies of time-variable deformation processes associated with active faults.

7. Acknowledgements

The authors thank Jack McGrath and Giulia Fedrizzi for assistance in the field, and Harri Williams and Richard Walshaw at Leeds Electron Microscopy and Spectroscopy Centre for their respective assistance with rock preparation and microprobe analysis. We also thank NatureScot for confirming that our sampling procedure (minimal, discrete sampling using a geological hammer) proposed for this study was appropriate given the Geological Conservation Review status of the location. This work was supported by the Leeds-York-Hull Natural Environment Research Council (NERC) Doctoral Training Partnership (DTP) Panorama under grant NE/S007458/1. Tim Craig thanks the Royal Society for support under URF/R1/180088. Tim Craig and Tim Wright were also supported through COMET, which is the NERC Centre for the Observation and Modelling of Earthquakes, Volcanoes and Tectonics, a partnership between UK Universities and the British Geological Survey.

8. Data Availability

Data will be made available on request.

9. Supplementary data

The following is the Supplementary data to this article:

Table S1: Summary of samples. BNG = British National Grid.

Sample, location (LX)	**Co-ordinates BNG**	**Distance from SZ**	**Domain**	**Fabric type / Strain**	**Strain (γ), Tatham and Casey 2007**	**EBSD & EDX**	**EMPA**
AS2239, L2	214920, 941664	500 m wall rock	1	Undeformed with respect to shear zone, bimodal grain size distribution (T0)	Outside of strain profile	X	X
AS2153, L4	215179, 941411	220 m	2	Low strain (T1)	Outside of strain profile	X	
AS2237, L5	215267, 941309	100 m	3	Low strain (T1)	< 0.5	Not included	
AS2161, L6	215306, 941259	0 m	4	Low strain (T1)	≥ 15	Not included	
AS2160, L6	215306, 941259	0 m	4	Medium strain (T2)	≥ 15	X	X
AS2158, L6	215306, 941259	0 m	4	High strain (T3) at contact with gneiss (AS2157)	≥ 15	X	
AS2240A, L1	214627, 941744	600 m wall rock	1	Wall rock but bimodal grain size through partial recrystallisation	Outside of strain profile	X	X
AS2151, L3	215085, 941472	Near SM1 340 m	2		Outside of strain profile	X	
AS2155, L5	215267, 941309	SM3 100 m	3	Low strain, 5 m from dyke margin	< 0.5	X	
AS2157, L6	215306, 941259	SM4 0 m	4	High strain at contact with dyke (AS2158)	≥ 15	X	X

For Tables S2-4, see attached file Supplementary data tables S2-4.xlsx.

References

Attfield, P., 1987. The structural history of the Canisp Shear Zone. Technical Report. URL: `http://sp.lyellcollection.org/`, doi:https://doi.org/10.1144/GSL.SP.1987.027.01.14.

Beach, A., 1973. The mineralogy of high temperature shear zones at Scourie, NW Scotland. Journal of Petrology 14, 231–248.

Beach, A., 1974a. Amphibolitization of Scourian granulites. Scottish Journal of Geology 10, 35–43.

Beach, A., 1974b. The measurement and significance of displacements on Laxfordian Shear Zones, North-West Scotland. Proceedings of the Geologists' Association 85, 13–IN1. doi:10.1016/S0016-7878(74)80032-5.

Beach, A., 1980. Retrogressive metamorphic processes in shear zones with special reference to the Lewisian complex. Journal of Structural Geology 2, 257–263. doi:10.1016/0191-8141(80)90058-9.

Beach, A., Coward, M.P., Graham, R.H., 1974. An interpretation of the structural evolution of the Laxford Front, north-west Scotland. Scottish Journal of Geology 9, 297–308. URL: `https://doi.org/10.1144/sjg09040297`, doi:10.1144/sjg09040297.

Bestmann, M., Prior, D.J., 2003. Intragranular dynamic recrystallization in naturally deformed calcite marble: diffusion accommodated grain boundary sliding as a result of subgrain rotation recrystallization. Journal of Structural Geology 25, 1597–1613. doi:10.1016/S0191-8141(03)00006-3.

Boland, J.N., Tullis, T.E., 1986. Deformation behavior of wet and dry clinopyroxenite in the brittle to ductile transition region. Mineral and rock deformation: Laboratory studies 36, 35–49.

Bons, P.D., Den Brok, B., 2000. Crystallographic preferred orientation development by dissolution–precipitation creep. Journal of Structural Geology 22, 1713–1722. doi:10.1016/S0191-8141(00)00075-4.

Bons, P.D., Elburg, M.A., Gomez-Rivas, E., 2012. A review of the formation of tectonic veins and their microstructures. Journal of structural geology 43, 33–62.

Brander, L., Svahnberg, H., Piazolo, S., 2012. Brittle-plastic deformation in initially dry rocks at fluid-present conditions: Transient behaviour of feldspar at mid-crustal levels. Contributions to Mineralogy and Petrology 163, 403–425. doi:10.1007/s00410-011-0677-5.

Bras, E., Baïsset, M., Yamato, P., Labrousse, L., 2021. Transient weakening during the granulite to eclogite transformation within hydrous shear zones (Holsnøy, Norway). Tectonophysics 819. doi:10.1016/j.tecto.2021.229026.

Bürgmann, R., Dresen, G., 2008. Rheology of the lower crust and upper mantle: Evidence from rock mechanics, geodesy, and field observations. Annual Review of Earth and Planetary Sciences 36, 531–567. doi:10.1146/annurev.earth.36.031207.124326.

Carreras, J., 2001. Zooming on Northern Cap de Creus shear zones. Journal of Structural Geology 23, 1457–1486. doi:10.1016/S0191-8141(01)00011-6.

Carreras, J., Casas, J.M., 1987. On folding and shear zone-development: a mesoscale structural study on the transition between two different tectonic styles. Tectonophysics 135, 87–98. doi:10.1016/0040-1951(87)90154-5.

Carreras, J., Estrada, A., White, S., 1977. The effects of folding on the c-axis fabrics of a quartz mylonite. Tectonophysics 39, 3–24.

Carter, N.L., Horseman, S.T., Russell, J.E., Handin, J., 1993. Rheology of rocksalt. Journal of Structural Geology 15, 1257–1271. doi:10.1016/0191-8141(93)90168-A.

Cartwright, I., 1990. Prograde metamorphism, anatexis, and retrogression of the Scourian complex, north-west Scotland, in: High-temperature metamorphism and crustal anatexis. Springer, pp. 371–399.

Chapman, H.J., Moorbath, S., 1977. Lead isotope measurements from the oldest recognised Lewisian gneisses of north-west Scotland. Nature 268, 41–42.

Clerc, C., Jolivet, L., Ringenbach, J.C., 2015. Ductile extensional shear zones in the lower crust of a passive margin. Earth and Planetary Science Letters 431, 1–7. doi:10.1016/J.EPSL.2015.08.038.

Corvò, S., Maino, M., Langone, A., Schenker, F.L., Piazolo, S., Casini, L., Seno, S., 2021. Local variations of metamorphic record from compositionally heterogeneous rocks (Cima di Gagnone, Central Alps): Inferences on exhumation processes of (U)HP–HT rocks. Lithos 390-391, 106126. doi:10.1016/J.LITHOS.2021.106126.

Corvò, S., Maino, M., Piazolo, S., Seno, S., Langone, A., 2022. Role of inherited compositional and structural heterogeneity in shear zone development at mid-low levels of the continental crust (the Anzola shear zone; Ivrea-Verbano Zone, Southern Alps). Lithos 422-423, 106745. doi:10.1016/J.LITHOS.2022.106745.

Coward, M.P., Potts, G.J., 1983. Complex strain patterns developed at the frontal and lateral tips to shear zones and thrust zones. Journal of Structural Geology 5, 383–399. URL: https://www.sciencedirect.com/science/article/pii/0191814183900251, doi:https://doi.org/10.1016/0191-8141(83)90025-1.

Cross, A.J., Skemer, P., 2019. Rates of Dynamic Recrystallization in Geologic Materials. Journal of Geophysical Research: Solid Earth 124, 1324–1342. doi:10.1029/2018JB016201.

Czaplińska, D., Piazolo, S., Zibra, I., 2015. The influence of phase and grain size distribution on the dynamics of strain localization in polymineralic rocks. Journal of Structural Geology 72, 15–32. doi:10.1016/J.JSG.2015.01.001.

Dell'Angelo, L.N., Tullis, J., 1996. Textural and mechanical evolution with progressive strain in experimentally deformed aplite. Tectonophysics 256, 57–82. doi:10.1016/0040-1951(95)00166-2.

Díaz Aspiroz, M., Lloyd, G.E., Fernández, C., 2007. Development of lattice preferred orientation in clinoamphiboles deformed under low-pressure metamorphic conditions. A SEM/EBSD study of metabasites from the

Aracena metamorphic belt (SW Spain). Journal of Structural Geology 29, 629–645. doi:10.1016/j.jsg.2006.10.010.

Dimanov, A., Rybacki, E., Wirth, R., Dresen, G., 2007. Creep and strain-dependent microstructures of synthetic anorthite–diopside aggregates. Journal of Structural Geology 29, 1049–1069. doi:10.1016/J.JSG.2007.02.010.

Droop, G., Fernandes, L., Shaw, S., 1999. Laxfordian metamorphic conditions of the Palaeoproterozoic Loch Maree Group, Lewisian Complex, NW Scotland. Scottish Journal of Geology 35, 31–50.

Drury, M.R., 2005. Dynamic recrystallization and strain softening of olivine aggregates in the laboratory and the lithosphere Rheology of olivine aggregates in the laboratory Low-strain rheology. Geological Society special publication 243, 143–158. doi:10.1144/GSL.SP.2005.243.01.11.

Evans, C.R., 1965. Geochronology of the Lewisian basement near Lochinver, Sutherland. Nature 207, 54–56.

Fagereng, A., Diener, J.F.A., Tulley, C.J., Manda, B., 2024. Metamorphic inheritance, lower-crustal earthquakes, and continental rifting. Geochemistry, Geophysics, Geosystems 25, e2023GC011305.

Fossen, H., Cavalcante, G.C.G., 2017. Shear zones – A review. Earth-Science Reviews 171, 434–455. doi:10.1016/J.EARSCIREV.2017.05.002.

Friend, C., Kinny, P., 2001. A reappraisal of the Lewisian Gneiss Complex: geochronological evidence for its tectonic assembly from disparate terranes in the Proterozoic. Contributions to Mineralogy and Petrology 142, 198–218.

Friend, C.R.L., Kinny, P.D., 1995. New evidence for protolith ages of Lewisian granulites, northwest Scotland. Geology 23, 1027–1030.

Fusseis, F., Regenauer-Lieb, K., Liu, J., Hough, R.M., De Carlo, F., 2009. Creep cavitation can establish a dynamic granular fluid pump in ductile shear zones. Nature 459, 974–977. doi:10.1038/nature08051.

Gardner, J., Wheeler, J., 2021. The influence of large second phase grains on microstructural evolution during diffusion creep. Journal of Structural Geology 148. doi:10.1016/j.jsg.2021.104371.

Gardner, R., Piazolo, S., Evans, L., Daczko, N., 2017a. Patterns of strain localization in heterogeneous, polycrystalline rocks – a numerical perspective. Earth and Planetary Science Letters 463, 253–265. doi:10.1016/J.EPSL.2017.01.039.

Gardner, R.L., Piazolo, S., Daczko, N.R., 2017b. Determining relative bulk viscosity of kilometre-scale crustal units using field observations and numerical modelling. Tectonophysics. 721, 275–291. doi:10.1016/j.tecto.2017.10.008.

Gerbi, C., Johnson, S.E., Shulman, D., Klepeis, K., 2016. Influence of microscale weak zones on bulk strength. Geochemistry, Geophysics, Geosystems 17, 4064–4077.

Getsinger, A.J., Hirth, G., 2014. Amphibole fabric formation during diffusion creep and the rheology of shear zones. Geology 42, 535–538. doi:10.1130/G35327.1.

Getsinger, A.J., Hirth, G., Stünitz, H., Goergen, E.T., 2013. Influence of water on rheology and strain localization in the lower continental crust. Geochemistry, geophysics, geosystems 14, 2247–2264. doi:10.1002/ggge.20148.

Giuntoli, F., Menegon, L., Warren, C.J., 2018. Replacement reactions and deformation by dissolution and precipitation processes in amphibolites. Journal of Metamorphic Geology 36, 1263–1286. doi:10.1111/jmg.12445.

Goddard, R.M., Hansen, L.N., Wallis, D., Stipp, M., Holyoke III, C.W., Kumamoto, K.M., Kohlstedt, D.L., 2020. A subgrain-size piezometer calibrated for EBSD. Geophysical Research Letters 47, e2020GL090056.

Gomez-Rivas, E., Butler, R.W., Healy, D., Alsop, I., 2020. From hot to cold - The temperature dependence on rock deformation processes: An introduction. Journal of Structural Geology 132, 103977. doi:10.1016/J.JSG.2020.103977.

Goodenough, K.M., Park, R.G., Krabbendam, M., Myers, J.S., Wheeler, J., Loughlin, S.C., Crowley, Q.G., Friend, C.R., Beach, A., Kinny, P.D., Graham, R.H., 2010. The Laxford shear zone: An end-Archaean terrane boundary? Geological Society Special Publication 335, 103–120. doi:10.1144/SP335.6.

Gratier, J.P., 1987. Pressure solution-deposition creep and associated tectonic differentiation in sedimentary rocks. Geological Society, London, Special Publications 29, 25–38.

Gratier, J.P., Dysthe, D.K., Renard, F., 2013. The Role of Pressure Solution Creep in the Ductility of the Earth's Upper Crust, in: Advances in Geophysics. Academic Press Inc.. volume 54, pp. 47–179. doi:10.1016/B978-0-12-380940-7.00002-0.

Gratier, J.P., Menegon, L., Renard, F., 2023. Pressure Solution Grain Boundary Sliding as a Large Strain Mechanism of Superplastic Flow in the Upper Crust. Journal of Geophysical Research: Solid Earth 128. doi:10.1029/2022JB026019.

Halfpenny, A., Prior, D.J., Wheeler, J., 2006. Analysis of dynamic recrystallization and nucleation in a quartzite mylonite. Tectonophysics 427, 3–14. doi:10.1016/J.TECTO.2006.05.016.

Hamilton, P.J., Evensen, N.M., O'nions, R.K., Tarney, J., 1979. Sm—Nd systematics of Lewisian gneisses: implications for the origin of granulites. Nature 277, 25–28.

Handy, M.R., 1994. Flow laws for rocks containing two non-linear viscous phases: a phenomenological approach. Journal of structural Geology 16, 287–301.

Henstock, T.J., Levander, A., Hole, J.A., 1997. Deformation in the lower crust of the San Andreas fault system in northern California. Science 278, 650–653.

Hirth, G., Kohlstedf, D., 2003. Rheology of the upper mantle and the mantle wedge: A view from the experimentalists. Geophysical monograph-american geophysical union 138, 83–106.

Hirth, G., Tullis, J., 1994. The brittle-plastic transition in experimentally deformed quartz aggregates. Journal of Geophysical Research: Solid Earth 99, 11731–11747.

Hussain, E., Wright, T.J., Walters, R.J., Bekaert, D.P., Lloyd, R., Hooper, A., 2018. Constant strain accumulation rate between major earthquakes on the North Anatolian Fault. Nature Communications 9. doi:10.1038/s41467-018-03739-2.

Ingleby, T., Wright, T.J., 2017. Omori-like decay of postseismic velocities following continental earthquakes. Geophysical Research Letters 44, 3119–3130. doi:10.1002/2017GL072865.

Ingles, J., Lamouroux, C., Soula, J.C., Guerrero, N., Debat, P., 1999. Nucleation of ductile shear zones in a granodiorite under greenschist facies conditions, Néouvielle massif, Pyrenees, France. Journal of Structural Geology 21, 555–576. doi:10.1016/S0191-8141(99)00042-5.

Jiang, Z., Prior, D.J., Wheeler, J., 2000. Albite crystallographic preferred orientation and grain misorientation distribution in a low-grade mylonite: implications for granular flow. Journal of Structural Geology 22, 1663–1674. doi:10.1016/S0191-8141(00)00079-1.

Kamb, W.B., 1959. Theory of Preferred Crystal Orientation Developed by Crystallization under Stress. The Journal of geology 67, 153–170. doi:10.1086/626571.

Karato, S.i., Wu, P., 1993. Rheology of the Upper Mantle: A Synthesis. Science (American Association for the Advancement of Science) 260, 771–778. doi:10.1126/science.260.5109.771.

Kaufmann, G., Amelung, F., 2000. Reservoir-induced deformation and continental rheology in vicinity of Lake Mead, Nevada. Journal of Geophysical Research 105, 16341–16358. doi:10.1029/2000JB900079.

Kenner, S.J., Segall, P., 2003. Lower crustal structure in northern California: Implications from strain rate variations following the 1906 San Francisco earthquake. Journal of Geophysical Research 108, 5–1. doi:10.1029/2001JB000189.

Kinny, P.D., Friend, C.R.L., 1997. U-Pb isotopic evidence for the accretion of different crustal blocks to form the Lewisian Complex of northwest Scotland. Contributions to Mineralogy and Petrology 129, 326–340. URL: `https://doi.org/10.1007/s004100050340`, doi:10.1007/s004100050340.

Kinny, P.D., Friend, C.R.L., Love, G.J., 2005. Proposal for a terrane-based nomenclature for the Lewisian gneiss complex of NW Scotland. Journal of the Geological Society 162, 175–186. doi:10.1144/0016-764903-149.

Kirby, S.H., 1985. Rock mechanics observations pertinent to the rheology of the continental lithosphere and the localization of strain along shear zones. Tectonophysics 119, 1–27. doi:10.1016/0040-1951(85)90030-7.

Knipe, R.J., 1989. Deformation mechanisms — recognition from natural tectonites. Journal of structural geology 11, 127–146. doi:10.1016/0191-8141(89)90039-4.

Kruse, R., Stünitz, H., 1999. Deformation mechanisms and phase distribution in mafic high-temperature mylonites from the Jotun Nappe, southern Norway. Tectonophysics 303, 223–249. doi:10.1016/S0040-1951(98)00255-8.

Lee, A.L., Stünitz, H., Soret, M., Battisti, M.A., 2022. Dissolution precipitation creep as a process for the strain localisation in mafic rocks. Journal of Structural Geology 155. doi:10.1016/j.jsg.2021.104505.

Lusk, A.D., Platt, J.P., 2020. The Deep Structure and Rheology of a Plate Boundary-Scale Shear Zone: Constraints from an Exhumed Caledonian Shear Zone, NW Scotland. Lithosphere 2020, 1–33. doi:10.2113/2020/8824736.

Malvoisin, B., Baumgartner, L.P., 2021. Mineral Dissolution and Precipitation Under Stress: Model Formulation and Application to Metamorphic Reactions. Geochemistry, Geophysics, Geosystems 22. doi:10.1029/2021GC009633.

Mandal, N., Kumar Samanta, S., Chakraborty, C., 2004. Problem of folding in ductile shear zones: a theoretical and experimental investigation. Journal of structural geology 26, 475–489. doi:10.1016/j.jsg.2003.07.004.

Mansard, N., Stünitz, H., Raimbourg, H., Précigout, J., 2020. The role of deformation-reaction interactions to localize strain in polymineralic rocks:

Insights from experimentally deformed plagioclase-pyroxene assemblages. Journal of Structural Geology 134. doi:10.1016/j.jsg.2020.104008.

Marti, S., Stünitz, H., Heilbronner, R., Plümper, O., Kilian, R., 2018. Syn-kinematic hydration reactions, grain size reduction, and dissolution-precipitation creep in experimentally deformed plagioclase-pyroxene mixtures. Solid Earth 9, 985–1009. doi:10.5194/se-9-985-2018.

McCaig, A., 1988. Deep fluid circulation in fault zones. Geology. 16, 867. doi:10.1130/0091-7613(1988)016¡0867:DFCIFZ¿2.3.CO;2.

McNamara, D.D., Wheeler, J., Pearce, M., Prior, D.J., 2012. Fabrics produced mimetically during static metamorphism in retrogressed eclogites from the Zermatt-Saas zone, Western Italian Alps. Journal of Structural Geology 44, 167–178.

McNamara, D.D., Wheeler, J., Pearce, M., Prior, D.J., 2024. A key role for diffusion creep in eclogites: Omphacite deformation in the Zermatt-Saas unit, Italian Alps. Journal of Structural Geology 179. doi:10.1016/j.jsg.2023.105033.

Menegon, L., Fusseis, F., Stünitz, H., Xiao, X., 2015. Creep cavitation bands control porosity and fluid flow in lower crustal shear zones. Geology. 43, 227–230. doi:10.1130/G36307.1.

Menegon, L., Pennacchioni, G., Spiess, R., 2008. Dissolution-precipitation creep of K-feldspar in mid-crustal granite mylonites. Journal of Structural Geology 30, 565–579. doi:10.1016/j.jsg.2008.02.001.

Mongkoltip, P., Ashworth, J.R., 1983. Exsolution of ilmenite and rutile in hornblende. The American mineralogist 68, 143–155.

Moorbath, S., Welke, H., Gale, N.H., 1969. The significance of lead isotope studies in ancient, high-grade metamorphic basement complexes, as exemplified by the Lewisian rocks of northwest Scotland. Earth and Planetary Science Letters 6, 245–256.

Moore, J., Beinlich, A., Piazolo, S., Austrheim, H., Putnis, A., 2020. Metamorphic Differentiation via Enhanced Dissolution along High Permeability Zones. Journal of petrology 61. doi:10.1093/petrology/egaa096.

Moore, J., Piazolo, S., Beinlich, A., Austrheim, H., Putnis, A., 2024. Brittle initiation of dissolution–precipitation creep in plagioclase-rich rocks: insights from the Bergen arcs, Norway. Contributions to Mineralogy and Petrology 179. doi:10.1007/s00410-024-02141-0.

Moore, J.D., Parsons, B., 2015. Scaling of viscous shear zones with depth-dependent viscosity and power-law stress-strain-rate dependence. Geophysical Journal International 202, 242–260. doi:10.1093/gji/ggv143.

Nieh, T.G., Wadsworth, J., 1997. Microstructural characteristics and deformation properties in superplastic intermetallics. Materials Science and Engineering: A 239-240, 88–96. URL: https://www.sciencedirect.com/science/article/pii/S0921509397005649, doi:https://doi.org/10.1016/S0921-5093(97)00564-9.

Orlandini, O.F., Mahan, K.H., 2020. Rheological evolution of a pseudotachylyte-bearing deep crustal shear zone in the western Canadian shield. Journal of Structural Geology 141. doi:10.1016/j.jsg.2020.104188.

Park, R.G., 1970. Observations on Lewisian chronology. Scottish Journal of Geology 6, 379–399.

Park, R.G., Tarney, J., 1987. The Lewisian complex: a typical Precambrian high-grade terrain? Evolution of the Lewisian and Comparable Precambrian High Grade Terrains 27, 13–25. doi:10.1144/GSL.SP.1987.027.01.03.

Passchier C, Trouw R, 2005. Microtectonics. Scholars Portal.

Peach, B.N., 1907. The geological structure of the North-West Highlands of Scotland. HM Stationery Office.

Pearce, M.A., Wheeler, J., 2014. Microstructural and Metamorphic Constraints on the Thermal Evolution of the Southern Region of the Lewisian Gneiss Complex, NW Scotland. Journal of Petrology 55, 2043–2066. doi:10.1093/petrology/egu049.

Pearce, M.A., Wheeler, J., Prior, D.J., 2011. Relative strength of mafic and felsic rocks during amphibolite facies metamorphism and deformation. Journal of Structural Geology 33, 662–675. doi:10.1016/j.jsg.2011.01.002.

Pennacchioni, G., Mancktelow, N.S., 2007. Nucleation and initial growth of a shear zone network within compositionally and structurally heterogeneous granitoids under amphibolite facies conditions. Journal of structural geology 29, 1757–1780. doi:10.1016/j.jsg.2007.06.002.

Piazolo, S., Bons, P.D., Jessell, M.W., Evans, L., Passchier, C.W., 2002. Dominance of microstructural processes and their effect on microstructural development: insights from numerical modelling of dynamic recrystallization. Deformation Mechanisms, Rheology and Tectonics: Current Status and Future Perspectives 200, 149–170. doi:10.1144/GSL.SP.2001.200.01.10.

Piazolo, S., Passchier, C.W., 2002. Controls on lineation development in low to medium grade shear zones: a study from the Cap de Creus peninsula, NE Spain. Journal of Structural Geology 24, 25–44. doi:10.1016/S0191-8141(01)00045-1.

Platt, J.P., Behr, W.M., Cooper, F.J., 2015. Metamorphic core complexes; windows into the mechanics and rheology of the crust. Journal of the Geological Society 172, 9–27. doi:10.1144/jgs2014-036.

Prior, D.J., Wheeler, J., Peruzzo, L., Spiess, R., Storey, C., 2002. Some garnet microstructures: an illustration of the potential of orientation maps and misorientation analysis in microstructural studies. Journal of structural geology 24, 999–1011. doi:10.1016/S0191-8141(01)00087-6.

Putnis, A., 2021. Fluid-Mineral Interactions: Controlling Coupled Mechanisms of Reaction, Mass Transfer and Deformation. Journal of Petrology 62. doi:10.1093/petrology/egab092.

Ramsay, J.G., Graham, R.H., 1970. Strain variation in shear belts. Canadian Journal of Earth Sciences 7, 786–813. URL: `https://doi.org/10.1139/e70-078`, doi:10.1139/e70-078.

Ranalli, G., 1995. Rheology of the earth. Chapman & Hall,, London :.

Ranalli, G., 1997. Rheology of the lithosphere in space and time. Geological Society special publication 121, 19–37. doi:10.1144/GSL.SP.1997.121.01.02.

Rutter, E.H., 1976. A Discussion on natural strain and geological structure - The kinetics of rock deformation by pressure solution. Philosophical transactions of the Royal Society of London. Series A: Mathematical and physical sciences 283, 203–219. doi:10.1098/rsta.1976.0079.

Rutter, E.H., Brodie, K.H., 1985. The Permeation of Water into Hydrating Shear Zones, in: Thompson, A.B., Rubie, D.C. (Eds.), Metamorphic Reactions: Kinetics, Textures, and Deformation. Springer New York, New York, NY, pp. 242–250. doi:10.1007/978-1-4612-5066-1-9.

Rutter, E.H., Brodie, K.H., 1988. The role of tectonic grain size reduction in the rheological stratification of the lithosphere. Geologische Rundschau 77, 295–307. URL: https://doi.org/10.1007/BF01848691, doi:10.1007/BF01848691.

Rutter, E.H., Holdsworth, R.E., Knipe, R.J., 2001. The nature and tectonic significance of fault-zone weakening: an introduction. Geological Society special publication 186, 1–11. doi:10.1144/GSL.SP.2001.186.01.01.

Rybacki, E., Dresen, G., 2000. Dislocation and diffusion creep of synthetic anorthite aggregates. Journal of Geophysical Research 105, 26017–26036. doi:10.1029/2000JB900223.

Schmid, S.M., Paterson, M.S., Boland, J.N., 1980. High temperature flow and dynamic recrystallization in carrara marble. Tectonophysics 65, 245–280. doi:10.1016/0040-1951(80)90077-3.

Segall, P., Simpson, C., 1986. Nucleation of ductile shear zones on dilatant fractures. Geology (Boulder) 14, 56–59. doi:10.1130/0091-7613(1986)14¡56:NODSZO¿2.0.CO;2.

Shannon, R.D., Rossi, R.C., 1964. Definition of topotaxy. Nature 202, 1000–1001.

Sibson, R.H., 1977. Fault rocks and fault mechanisms. Journal of the Geological Society. 133, 191–213. doi:10.1144/gsjgs.133.3.0191.

Sibson, R.H., 1981. Fluid flow accompanying faulting: field evidence and models. Earthquake prediction: an international review 4, 593–603.

Sibson, R.H., 1994. Crustal stress, faulting and fluid flow. Geological Society, London, Special Publications 78, 69–84.

Sills, J.D., 1982. The retrogression of ultramafic granulites from the Scourian of NW Scotland. Mineralogical Magazine 46, 55–61.

Smith, J.R., Piazolo, S., Daczko, N.R., Evans, L., 2015. The effect of pre-tectonic reaction and annealing extent on behaviour during subsequent deformation: insights from paired shear zones in the lower crust of Fiordland, New Zealand. Journal of metamorphic geology 33, 557–577. doi:10.1111/jmg.12132.

Sorensen, K., 1983. Growth and dynamics of the Nordre Stromfjord shear zone. Journal of Geophysical Research 88, 3419–3437. doi:10.1029/JB088iB04p03419.

Soret, M., Agard, P., Ildefonse, B., Dubacq, B., Prigent, C., Rosenberg, C., 2019. Deformation mechanisms in mafic amphibolites and granulites: Record from the Semail metamorphic sole during subduction infancy. Solid Earth 10, 1733–1755. doi:10.5194/se-10-1733-2019.

Steffen, K., Selverstone, J., Brearley, A., 2001. Episodic weakening and strengthening during synmetamorphic deformation in a deep-crustal shear zone in the Alps. Geological Society, London, Special Publications 186, 141–156.

Stenvall, C.A., Fagereng, A., Diener, J.F., 2019. Weaker Than Weakest: On the Strength of Shear Zones. Geophysical Research Letters 46, 7404–7413. doi:10.1029/2019GL083388.

Stenvall, C.A., Fagereng, A., Diener, J.F.A., Harris, C., Janney, P.E., 2020. Sources and Effects of Fluids in Continental Retrograde Shear Zones: Insights from the Kuckaus Mylonite Zone, Namibia. Geofluids. 2020, 1–21. doi:10.1155/2020/3023268.

Stipp, M., Stünitz, H., Heilbronner, R., Schmid, S.M., 2002. Dynamic recrystallization of quartz: correlation between natural and experimental conditions. Deformation Mechanisms, Rheology and Tectonics: Current Status and Future Perspectives 200, 171–190. doi:10.1144/GSL.SP.2001.200.01.11.

Stokes, M.R., Wintsch, R.P., Southworth, C.S., 2012. Deformation of amphibolites via dissolution-precipitation creep in the middle and lower crust. Journal of Metamorphic Geology 30, 723–737. doi:10.1111/j.1525-1314.2012.00989.x.

Stünitz, H., Neufeld, K., Heilbronner, R., Finstad, A.K., Konopásek, J., Mackenzie, J.R., 2020. Transformation weakening: Diffusion creep in eclogites as a result of interaction of mineral reactions and deformation. Journal of Structural Geology 139, 104129.

Stünitz, H., Tullis, J., 2001. Weakening and strain localization produced by syn-deformational reaction of plagioclase. International Journal of Earth Sciences 90, 136–148.

Sutton, J., Watson, J., 1950. The pre-Torridonian metamorphic history of the Loch Torridon and Scourie areas in the North-West Highlands, and its bearing on the chronological classification of the Lewisian. The Quarterly journal of the Geological Society of London. 106, 241–307. doi:10.1144/GSL.JGS.1950.106.01-04.16.

Svahnberg, H., Piazolo, S., 2010. The initiation of strain localisation in plagioclase-rich rocks: Insights from detailed microstructural analyses. Journal of structural geology 32, 1404–1416. doi:10.1016/j.jsg.2010.06.011.

Takeuchi, C.S., Fialko, Y., 2012. Dynamic models of interseismic deformation and stress transfer from plate motion to continental transform faults. Journal of Geophysical Research: Solid Earth 117, n/a. doi:10.1029/2011JB009056.

Tarney, J., 1963. Assynt dykes and their metamorphism. Nature 199, 672–674.

Tatham, D.J., Casey, M., 2007. Inferences from shear zone geometry: an example from the Laxfordian shear zone at Upper Badcall, Lewisian Complex, NW Scotland. Deformation of the Continental Crust: The Legacy of Mike Coward 272, 47–57. doi:10.1144/GSL.SP.2007.272.01.04.

Teall, J.J.H., 1885. The Metamorphosis of Dolerite into Hornblende-schist. Quarterly journal of the Geological Society of London 41, 133–145. doi:10.1144/GSL.JGS.1885.041.01-04.19.

Tian, Z., Freymueller, J.T., Yang, Z., 2020. Spatio-temporal variations of afterslip and viscoelastic relaxation following the Mw 7.8 Gorkha (Nepal) earthquake. Earth and Planetary Science Letters 532, 116031. doi:10.1016/J.EPSL.2019.116031.

Tokle, L., Hirth, G., 2021. Assessment of Quartz Grain Growth and the Application of the Wattmeter to Predict Quartz Recrystallized Grain Sizes. Journal of geophysical research. Solid earth 126, n/a. doi:10.1029/2020JB021475.

Trimby, P.W., Prior, D.J., Wheeler, J., 1998. Grain boundary hierarchy development in a quartz mylonite. Journal of structural geology 20, 917–935. doi:10.1016/S0191-8141(98)00026-1.

Twiss, R.J., 1977. Theory and applicability of a recrystallized grain size paleopiezometer. Pure and applied geophysics 115, 227–244. doi:10.1007/BF01637105.

Viegas, G., Menegon, L., Archanjo, C., 2016. Brittle grain-size reduction of feldspar, phase mixing and strain localization in granitoids at mid-crustal conditions (Pernambuco shear zone, NE Brazil). Solid earth (Göttingen) 7, 375–396. doi:10.5194/se-7-375-2016.

Warren, J.M., Hirth, G., 2006. Grain size sensitive deformation mechanisms in naturally deformed peridotites. Earth and planetary science letters 248, 438–450. doi:10.1016/j.epsl.2006.06.006.

Wassmann, S., Stöckhert, B., 2013. Rheology of the plate interface - Dissolution precipitation creep in high pressure metamorphic rocks. doi:10.1016/j.tecto.2013.09.030.

Weiss, J.R., Qiu, Q., Barbot, S., Wright, T.J., Foster, J.H., Saunders, A., Brooks, B.A., Bevis, M., Kendrick, E., Ericksen, T.L., Avery, J., Smalley, R., Cimbaro, S.R., Lenzano, L.E., Barón, J., Báez, J.C., Echalar, A., 2019. Illuminating subduction zone rheological properties in the wake of a giant earthquake. Science Advances 5, eaax6720. URL: https://doi.org/10.1126/sciadv.aax6720, doi:10.1126/sciadv.aax6720.

Wenk, H.R., Yu, R., Cárdenes, V., Lopez-Sanchez, M.A., Sintubin, M., 2020. Fabric and anisotropy of slates: From classical studies to new results. Journal of Structural Geology 138, 104066. doi:10.1016/J.JSG.2020.104066.

Wheeler, J., 1992. Importance of pressure solution and coble creep in the deformation of polymineralic rocks. Journal of Geophysical Research:

Solid Earth 97, 4579–4586. URL: https://doi.org/10.1029/91JB02476, doi:https://doi.org/10.1029/91JB02476.

Whitney, D.L., Evans, B.W., 2010. Abbreviations for names of rock-forming minerals. The American mineralogist 95, 185–187. doi:10.2138/am.2010.3371.

Wightman, R.H., Prior, D.J., Little, T.A., 2006. Quartz veins deformed by diffusion creep-accommodated grain boundary sliding during a transient, high strain-rate event in the Southern Alps, New Zealand. Journal of structural geology 28, 902–918. doi:10.1016/j.jsg.2006.02.008.

Williams, R.T., Fagereng, A., 2022. The role of quartz cementation in the seismic cycle: A critical review. Reviews of Geophysics 60, e2021RG000768.

Wintsch, R.P., Wathen, B.A., McAleer, R.J., Walters, J., Matthews, J.A., 2024. Deformation by Pressure Solution and Grain Boundary Sliding in a Retrograde Shear Zone in Southern New England, USA. American Journal of Science 324. URL: https://ajsonline.org/article/125064-deformation-by-pressure-solution-and-grain- doi:10.2475/001c.125064.

Wintsch, R.P., Yi, K., 2002. Dissolution and replacement creep: a significant deformation mechanism in mid-crustal rocks. Journal of structural geology 24, 1179–1193. doi:10.1016/S0191-8141(01)00100-6.

Woodcock, N., Mort, K., 2008. Classification of fault breccias and related fault rocks. Geological magazine. 145, 435–440. doi:10.1017/S0016756808004883.

Yamasaki, T., Wright, T.J., Houseman, G.A., 2014. Weak ductile shear zone beneath a major strike-slip fault: Inferences from earthquake cycle model constrained by geodetic observations of the western North Anatolian Fault Zone. Journal of geophysical research. Solid earth 119, 3678–3699. doi:10.1002/2013JB010347.